

Site-specific gains and losses of heterochromatin accelerate the age-related neurodegeneration through the cascading destruction of KDM3B-centered epigenomic network

Mi-Jin An

Chung-Ang University

Ji-Young Kim

Jinhong Park

Chung-Ang University

Jinho Kim

Chung-Ang University

Dae-Hyun Kim

Chung-Ang University

Geun-Seup Shin

Chung-Ang University

Hyun-Min Lee

Chung-Ang University

Ah-Ra Jo

Chung-Ang University

Chul-Hong Kim

Chung-Ang University

Mi Jin Kim

Chung-Ang University

Jeongkyu Kim

Chung-Ang University

Sangmyung Rhee

Chung-Ang University

Sang-Beom Seo

Chung-Ang University

Jung-Woong Kim (✉ jungkim@cau.ac.kr)

Chung-Ang University <https://orcid.org/0000-0003-4458-7213>

Keywords: heterochromatin, aging, Kdm3b, epigenome, network, retina, homeostasis, cone photoreceptor, synapse, apoptosis

Posted Date: January 14th, 2022

DOI: <https://doi.org/10.21203/rs.3.rs-1246914/v1>

License: © ⓘ This work is licensed under a Creative Commons Attribution 4.0 International License.

[Read Full License](#)

1 **Site-specific gains and losses of heterochromatin accelerate the age-related**
2 **neurodegeneration through the cascading destruction of KDM3B-centered epigenomic**
3 **network**

4
5 Mi-Jin An^{1,2}, Ji-Young Kim^{1,2}, Jinhong Park¹, Jinho Kim¹, Dae-Hyun Kim¹, Geun-Seup Shin¹, Hyun-Min
6 Lee¹, Ah-Ra Jo¹, Chul-Hong Kim¹, Mi Jin Kim¹, Jeongkyu Kim¹, Sangmyung Rhee¹, Sang-Beom Seo¹ and
7 Jung-Woong Kim^{1,*}

8

9 ¹Department of Life Science, Chung-Ang University, Seoul 06974, South Korea

10 ²These authors contributed equally: Mi-Jin An, Ji-Young Kim

11 e-mail: M-J. An, dksalwls333@gmail.com; J-Y. Kim, jykim@cau.ac.kr

12

13

14 **Keywords:**

15 heterochromatin, aging, Kdm3b, epigenome, network, retina, homeostasis, cone photoreceptor, synapse,
16 apoptosis

17

18

19

20

21 ***Corresponding author:**

22 Jung-Woong Kim, Ph.D., Professor

23 Department of Life Science, Chung-Ang University, Seoul 06974, South Korea

24 Tel: +82-2-820-6682, Fax: +82-2-815-6682

25 Email: jungkim@cau.ac.kr

26 **ABSTRACT**

27 Epigenetic alterations explained by the “loss of heterochromatin” model have been proposed as a universal
28 mechanism of aging, but the region-specific changes of heterochromatin during aging are unclear. Here, we
29 examine age-dependent transcriptomic profiling of mouse retinal neurons to identify epigenetic regulators
30 involved in heterochromatin loss. RNA sequencing analysis revealed gradual down-regulation of *Kdm3b*
31 during retinal aging. Disruption of *Kdm3b* (*Kdm3b*^{+/-}) in 12-month-old mouse retina decreased the number
32 of cone photoreceptors and changed the morphology of cone ribbon synapses. Integration of transcriptome
33 profiling with epigenomic analysis demonstrated gain of heterochromatin feature in synapse assembly and
34 vesicle transport genes via the accumulation of H3K9 mono- and di-methylation. However, the loss of
35 heterochromatin in apoptotic genes exacerbated retinal neurodegeneration. We propose that this KDM3B-
36 centered epigenomic network is crucial for maintaining cone photoreceptor homeostasis via the modulation
37 of gene-set specific heterochromatin features during aging.

38 **INTRODUCTION**

39 Aging affects all organ systems, but age-related nervous system deficits are among the most prominent
40 aging-related changes. Neuronal functions are gradually impaired during aging via aberrant neuronal
41 network activity, increased oxidative stress, and disturbed energy homeostasis¹. The retina exhibits
42 elaborate cellular patterns and circuitry and is one of the best-understood models of the vertebrate central
43 nervous system; the differentiated retina, a functional aging model, is suitable for demonstrating the
44 destruction between physical neuronal networks (synapses) and molecular regulatory². Retinal aging leads
45 to a reduction in visual acuity and visual field sensitivity, and an increased dark adaptation threshold,
46 resulting in age-related diseases, such as age-related macular degeneration (AMD). Although these
47 physiological changes are apparent, the molecular mechanisms underlying neurochemical changes and
48 genome-wide epigenetic homeostasis during aging have not been identified.

49 Epigenetic regulation directly contributes to aging and age-related diseases, including changes in
50 chromatin accessibility, accumulation of histone variants, aberrant histone modifications, and chromatin
51 organization³. The “loss of heterochromatin” is considered a common mechanism of aging across cell types
52 and species. Age-related destabilization of tightly compacted chromatin leads to aberrant gene expression
53 and cellular dysfunction. A typical mark of constitutive heterochromatin is the trimethylation of histone H3
54 on lysine 9 (H3K9me3), while H3K27me3 is usually enriched in facultative heterochromatin⁴. Aging-
55 associated losses of repressive histone mark occur at H3K9me3 and H3K27me3. For example, histone
56 methyl transferase SUV39H1 expression levels in hematopoietic stem cells decrease during aging, resulting
57 in a global reduction in H3K9me3 level and perturbed heterochromatin function⁵. In addition, EZH2 is
58 downregulated in stressed and senescent human lung cells, leading H3K27me3 loss⁶. However, the region-
59 specific changes in heterochromatin of the functionally active genes in differentiated cells have not been
60 elucidated.

61 The epigenomic network is controlled by chromatin modification and the binding of transcription
62 factors, resulting in changes in gene expression. The resulting variability in the pattern of epigenetic

63 information within individual cells in a population during aging leads to transcriptional drifts and genomic
64 instability. Histone-modifying enzymes are regulatory factors for gene expression; among them, histone
65 lysine methyl transferases and demethylases (KDMs) establish functional cell types through dynamic
66 writing and erasing methylation marks on cell-type specific gene elements during development and aging^{7,8}.
67 The lysine-specific demethylase 3 (KDM3) family includes KDM3A, KDM3B, and KDM3C, which are
68 specific demethylases for mono-, and di-methylation at H3K9 and act as transcriptional activators⁹. The
69 KDM3 family is crucial for cell survival and proliferation in rapidly dividing cells, such as prostate cancer,
70 leukemia, and hepatocellular carcinoma cells⁹⁻¹¹. Nevertheless, whether and how KDM3 contributes to non-
71 mitotic differentiated cells in development, aging, and disease development is still poorly understood.

72 The functional physiology of differentiated cells is manifested through genetically encoded
73 molecular interactions and complex networks. Multi-dimensional epigenomic networks can shed light on
74 gene regulatory networks (GRNs) in *in vivo* systems, resulting in the visualization of hidden biomolecular
75 interactions. GRNs reveal cell-type specific development, differentiation, and cellular functions that control
76 the transcriptional expression of signal molecules and transcription factors, and regulatory interactions^{12,13}.
77 The network structure of integrated genomes and epigenomes contributes to better understanding of spatial
78 and temporal regulation of gene expression during development and aging¹⁴. It is also possible to measure
79 the network strength of gene regulation-epigenetic modification via the perpetual imbalance of homeostasis
80 during aging.

81 Herein, we aimed to understand these epigenomic networks using genetic approaches, integrated
82 with physiological assays and multiple genome-wide analyses using fully differentiated retina as an aging
83 model system. We found that haploinsufficiency of *Kdm3b* is associated with a decreased number of cone
84 photoreceptors via increased apoptosis and induced alterations of cone ribbon synapses due to the site-
85 specific alteration of heterochromatin features. Furthermore, KDM3B is required for the maintenance of
86 the integrated GRN that confers normal homeotic regulation in the mouse retina during aging.

87 **RESULTS**

88 **Characterization of heterochromatin organization and transcriptomic profile involved in retinal**

89 **aging.** The retina is composed of six neuronal cell types, including rod and cone photoreceptors (Fig. 1a).

90 To investigate the organization pattern of chromatin during retinal aging, we observed the distribution of

91 heterochromatin in the nuclei of photoreceptors using DAPI staining. Heterochromatin was detected at the

92 nuclear periphery and within chromocenters in cone photoreceptors of 2-month-old mice, but less

93 condensed heterochromatin was observed in the center of the nucleus in 18-month-old mice (Fig. 1b).

94 However, the distribution of heterochromatin did not change in the rods of both 2- and 18-month-old mice.

95 The number and mean area of chromocenters in cone nuclei decreased in the 18-month-old mice compared

96 to that in the 2-month-old mice (Fig. 1c and Extended Data Fig. 1a). Several studies have shown that

97 repressive histone modifications, such as H3K9me2/3, are hallmarks of pericentromeric heterochromatin

98 that play a pivotal role in heterochromatin formation^{15,16}. We also observed the distribution of silencing

99 histone modification (H3K9me1/2/3) and active modification (H3K9ac and H3K4me3) in cones and rods

100 during aging. H3K9me2/3 was abundant in the heterochromatin at the nuclear periphery in 2-month-old

101 mice with conventional nuclear architecture, whereas H3K9me2/3 showed unusual distribution in both

102 euchromatin and heterochromatin (but not in chromocenters) in 18-month-old mice (Extended Data Fig.

103 1b). We did not observe any differences in the distributions of H3K9me1 and active modification between

104 2-month-old mice and 18-month-old mice (Extended Data Fig. 1b). Furthermore, we confirmed the global

105 histone modification of whole retina using immunoblotting (Extended Data Fig. 1c). H3K9me2 level was

106 slightly decreased in 18-month-old mice, whereas H3K9me3 level was increased in whole retina of 18-

107 month-old mice. These data indicate that genome-wide organization of chromatin is altered during retina

108 aging.

109 To investigate whether epigenetic regulators are involved in “loss of heterochromatin features”

110 during neuronal aging, we performed gene expression profiling using RNA-sequencing analysis of 1-, 6-,

111 12-, and 18-month-old mice retina. Strong agreement was observed between the results of each biological
112 replicate from the different time points (Extended Data Fig. 2a). Given the criteria of FPKM > 30.0 and
113 coefficient of variation between each biological replicate within 20%, 1,615 differentially expressed
114 transcripts (DETs) were obtained by pairwise comparisons of the samples (Fig. 1d, Extended Data Fig. 2b
115 and Supplementary Table 1). We performed a K-means clustering analysis of DETs with $k = 10$ (Fig. 1e,f
116 and Extended Data Fig. 2c). Ten main clusters of expression patterns were discerned. We focused on cluster
117 8 and 9, which represented transcripts that are gradually downregulated during aging and included genes
118 that are important in chromatin remodeling, such as *Kdm3b*, *Kdm5b*, *Kmt2e*, and *Park7* (Fig. 1e, Extended
119 Data Fig. 2d and Supplementary Table 2). Interestingly, histone H3K9me1/2 demethylase *Kdm3b* is
120 correlated with the abnormalities of human eye, including nystagmus, low vision, and learning of
121 cerebellum-dependent optokinetic response (OKR)¹⁷. We confirmed that KDM3B mRNA and protein levels
122 were approximately 25% decreased in 18-month-old mice compared to that in 2-month-old mice (Fig. 1g,
123 h). Furthermore, KDM3B was highly expressed in heterochromatin and chromocenters in 2-month-old mice,
124 whereas KDM3B level decreased in heterochromatin and chromocenters in 18-month-old mice (Extended
125 Data Fig. 3a). Collectively, these results suggest that KDM3B may be crucial for the regulation of
126 heterochromatin feature in mice retina during aging.

127

128 **Abnormal eye phenotypes in *Kdm3b*^{+/-} mice.** To determine the cellular and molecular functions of
129 KDM3B in the retina, we generated *Kdm3b* functional knock-out mice via the gene trap technique
130 (Extended Data Fig. 3b, c, and Supplementary note). We confirmed that the KDM3B mRNA and protein
131 levels were reduced by approximately 50% to 80% in *Kdm3b*^{+/-} mouse retinas (Extended Data Fig. 3d, e,
132 respectively). Additionally, publicly available mRNA-sequencing data (GSE 74660) of mouse retinal tissue
133 showed that *Kdm3b* expression continued to increase up to stage P28 in whole retina and cones (Extended
134 Data Fig. 3f). We found that KDM3B is highly enriched in the nucleus of cones, using
135 immunohistochemistry (IHC), suggesting that it plays a role in the development or maintenance of cellular

136 functions in cone photoreceptor cells (Extended Data Fig. 3g).

137 To demonstrate the functional role of *Kdm3b* in the eye, we observed the morphology and the
138 structure of the enucleated eyeball and retinal tissue. We clearly detected smaller eyes and abnormal corneal
139 phenotypes in 12-month-old *Kdm3b*^{+/-} mice compared to those in 1-month-old mice (Extended Data Fig.
140 3h). To investigate the structural and morphological differences in the retina, we measured the thickness of
141 the entire retinas of 1-, 6-, and 12-month-old *Kdm3b*^{+/+} and *Kdm3b*^{+/-} mice. The retinal outer nuclear layer
142 (ONL) of the *Kdm3b*^{+/-} mice was thinner than that of the *Kdm3b*^{+/+} mice (Fig. 2a, and Supplementary Fig.
143 1a,b). The mean ONL thickness of *Kdm3b*^{+/-} mice was significantly reduced in 12-month-old mice (1,600
144 μm inferior: $97 \pm 10 \mu\text{m}$ versus $57 \pm 2.95 \mu\text{m}$, 1,600 μm superior: $84.6 \pm 9.35 \mu\text{m}$ versus $54.7 \pm 2 \mu\text{m}$) (Fig.
145 2b). However, there was no difference between the mean ONL thickness of 1-month-old *Kdm3b*^{+/+} and
146 *Kdm3b*^{+/-} mice (Fig. 2a, b). Consistent with these results, we observed that the number of nuclei in the ONL
147 was markedly reduced in *Kdm3b*^{+/-} mouse retinas among both 6-month-old (266 ± 3.06 versus 239 ± 2.34
148 nuclei/ $100 \mu\text{m}^2$, $P = 1.93\text{E-}5$) and 12-month-old mice (239 ± 3.38 versus 205.1 ± 3.27 nuclei/ $100 \mu\text{m}^2$, $P =$
149 $9.0\text{E-}6$) (Fig. 2c). We also observed that the mean thickness of the inner nuclear layer (INL) and the number
150 of nuclei in the INL and ganglion cell layer (GCL) were decreased in 1- and 6-month-old mice (Extended
151 Data Fig. 4a, b). The decrease in ONL thickness in the *Kdm3b*^{+/-} retina could be because of reduced number
152 of photoreceptor cell nuclei, including those of the rods and cones. To determine whether the rod and cone
153 populations decreased in the ONL of the *Kdm3b*^{+/-} retina, we performed IHC with cone-cell specific (anti-
154 CAR; cone arrestin) and rod-cell specific (anti-RHO; rhodopsin) antibodies. We found that *Kdm3b*
155 haploinsufficiency induced different morphologies and reduced the number of cones (14.6 ± 0.41 versus
156 9.8 ± 0.26 cones/ $100 \mu\text{m}^2$ $P = 4.93\text{E-}34$) in 12-month-old mice, but it was not associated with differences
157 in the rods (Fig. 2d, and Extended Data Fig. 4c).

158 Vertebrate rod and cone photoreceptors include outer segments (OS) and cell bodies that contribute
159 to phototransduction, are required for cell viability, and a synaptic terminal able to signal to second-order
160 neurons¹⁸. To determine the progression of cone loss in aged *Kdm3b*^{+/-} retinas, we examined the density of

161 cones and the morphological changes of cone OS by immunostaining analysis of whole mouse retinas.
162 Consistent with that of retina sections, the mean number of cones was significantly decreased in 12-month-
163 old *Kdm3b*^{+/-} mouse retinas, but the mean diameter of the cone-cell bodies was not significantly different
164 between *Kdm3b*^{+/+} and *Kdm3b*^{+/-} mice (Fig. 2e, and Supplementary Fig. 1c,d). The mean length of the inner
165 segment of cones was significantly decreased in 12-month-old *Kdm3b*^{+/-} mouse retinas (Fig. 2f). However,
166 the mean circumference of the cone OS was similar between *Kdm3b*^{+/+} and *Kdm3b*^{+/-} mouse retinas (Fig.
167 2f). Even though the overall mean cone lengths were similar, the mean lengths of the basal side and cone-
168 cell body in the *Kdm3b*^{+/-} mouse retinas were longer than those of the *Kdm3b*^{+/+} mouse retinas (Extended
169 Data Fig. 4d). Interestingly, we observed that the mean presynaptic area of cones (pedicle) was smaller in
170 the 12-month-old *Kdm3b*^{+/-} mouse retinas (Fig. 2g, and Supplementary Fig. 1e). These results suggest that
171 *Kdm3b* haploinsufficiency induced morphological changes and loss of cone photoreceptors in the aged
172 mouse retina.

173

174 **Transcriptomic profiling of *Kdm3b*^{+/-} mouse retinas.** After determining the morphological changes in the
175 *Kdm3b*^{+/-} mouse retinas, we analyzed differential transcript expression in *Kdm3b*^{+/-} retina. We performed
176 transcriptome profiling of 12-month-old *Kdm3b*^{+/+} and *Kdm3b*^{+/-} mouse retinas by RNA-sequencing
177 analysis. Principal component analysis (PCA) plot showed that *Kdm3b*^{+/-} retinas accounted for the largest
178 variance, and biological replicates showed great reproducibility (Fig. 3a). Volcano plots present the
179 statistical significance of differential transcript expressions with respective fold-changes ($P < 0.05$, absolute
180 \log_2 fold-change (\log_2 FC) > 0.5) compared to the expression observed in the control group (Fig. 3b).
181 Application of DEseq with conservative access to the RNA-sequencing data gained from the *Kdm3b*^{+/-}
182 retinal samples confirmed 3,978 differentially expressed transcripts (Fig. 3c and Supplementary Table 3).
183 The significant upregulation or downregulation of approximately 20% genes was revealed in the *Kdm3b*^{+/-}
184 retina (19,485 annotated transcripts, Extended Data Fig. 5a). Gene ontology (GO) analysis was performed
185 to reveal the biological connection among the upregulated (1,814 genes) and downregulated (1,852 genes)

186 DEGs in *Kdm3b*^{+/-} mouse retinas (Fig. 3d and Supplementary Table 4). Clustering of the upregulated DEGs
187 in *Kdm3b*^{+/-} retinas enabled their classification into several categories that were associated with mRNA
188 splicing and DNA damage stimuli, and downregulated DEGs were involved in synapse assembly and
189 vesicle transport (Fig. 3d). Gene set enrichment analysis (GSEA), which shows the biological pathways
190 and processes of the DEGs, also revealed that genes associated with cellular responses to DNA damage
191 stimuli and apoptotic processes were upregulated, while the repressed genes in *Kdm3b*^{+/-} mouse retinas were
192 involved in synapse assembly and vesicle-mediated transport (Fig. 3e). The selected genes in these groups
193 were upregulated or downregulated in *Kdm3b*^{+/-} mouse retinas, indicating that KDM3B has a crucial role in
194 cell death and synaptic transmission in the mouse retina (Fig. 3f, g). Since KDM3B haploinsufficiency
195 induced the expression of gene sets for mRNA splicing, we also investigated alternative splicing events in
196 RNA-sequencing data. The identified splice-site variants were categorized as 3,038 events for skipped exon
197 (SE), 387 events for 5'-splice site (5'-SS), 642 events for 3'-splice site (3'-SS), 342 events for mutually
198 exclusive exon (ME), and 906 events for retained intron (RI) (Extended Data Fig. 5b). These events showed
199 the distribution of protein-coding genes (Extended Data Fig. 5c). RI is retained by the glycolytic enzyme,
200 Aldolase A (*Aldoa*). The *Aldoa* transcript in *Kdm3b*^{+/+} mice did not include any introns between exon 3 and
201 exon 5; however, the introns were not spliced in the *Kdm3b*^{+/-} mouse retinas, suggesting a novel effect of
202 KDM3B in transcript maturation (Extended Data Fig. 5d). These results showed that KDM3B ablation
203 selectively regulated the expression of gene sets involved in neuronal apoptosis and synaptic transmission.

204

205 **Induction of apoptotic signals in aged *Kdm3b*^{+/-} mouse retinas.** Previous studies suggested that apoptosis
206 occurs in pathologic photoreceptor cell death in several mouse models of retinal degeneration¹⁹. Since the
207 number of cone photoreceptors was reduced in *Kdm3b*^{+/-} aged mice, we investigated whether retinal cells
208 in the ONL were damaged due to the death of photoreceptors. We detected the presence of Müller glial cells,
209 which are involved in the clearance of damaged cells and retinal regeneration, using anti-GFAP antibodies.
210 The mean Müller cell counts were significantly increased in 6- and 12-month-old *Kdm3b*^{+/-} retinas

211 compared to that in age-matched *Kdm3b*^{+/+} retinas (Fig. 4a, and Extended Data Fig. 6a). To further confirm
212 whether retinal cell damage induces photoreceptor cell death through apoptosis, we stained 1- and 12-
213 month-old *Kdm3b*^{+/+} and *Kdm3b*^{+/-} retinas with the executive apoptotic marker, cytochrome c. The intensity
214 of cytochrome c was significantly increased in 12-month-old *Kdm3b*^{+/-} retinas compared to that in 1-month-
215 old *Kdm3b*^{+/-} retinas. However, this was not observed in 12- and 1-month-old *Kdm3b*^{+/+} retinas (Fig. 4b).
216 Interestingly, we observed an increased release of cytochrome c in the cones of 12-month-old *Kdm3b*^{+/-}
217 retinas (Fig. 4c, and Supplementary Fig. 2a). Furthermore, we used TUNEL staining to determine whether
218 degenerating cone photoreceptors underwent apoptosis through gDNA fragmentation. TUNEL-positive
219 apoptotic cones also markedly increased in 12-month-old *Kdm3b*^{+/-} retinas (Fig. 4d, Extended Data Fig. 6b,
220 and Supplementary Fig. 2b). Cytochrome c and TUNEL-positive signals were densely detected in the
221 outermost ONL, where most of the cone photoreceptors are located in the retina (Fig. 4c, d). To explore the
222 potential molecular mechanism that mediated KDM3B-induced apoptosis, we investigated the levels of
223 apoptosis-associated proteins using a mouse apoptosis antibody array. Several apoptosis-associated proteins
224 were upregulated or downregulated in 8-month-old *Kdm3b*^{+/-} retina (Fig. 4e, f, and Extended Data Fig. 6c,
225 d). Compared to that in the *Kdm3b*^{+/+} retina, the expression of pro-apoptotic molecules, such as Bad,
226 increased by 20% in 8-month-old *Kdm3b*^{+/-} retina (Fig. 4e). Therefore, *Kdm3b* haploinsufficiency
227 upregulated apoptotic signals in cone photoreceptors.

228

229 **Synaptic functional morphology of cone photoreceptors in *Kdm3b*^{+/-} mouse retinas.** Photoreceptor
230 ribbon synapses are specialized synaptic structures in the outer plexiform layer, where visual signals are
231 transmitted from photoreceptors to bipolar and horizontal cells²⁰. Since functional KDM3B is required for
232 the expression of synaptic and vesicle transport gene sets, we examined whether *Kdm3b* haploinsufficiency
233 affected changes in the functional morphology of cone ribbon synapses. The mean area of cone synaptic
234 terminals and the number of ribbon synapses was significantly reduced in 12-month-old *Kdm3b*^{+/-} retinas
235 (Fig. 5a, Supplementary Fig. 3, and Supplementary video). Furthermore, we performed transmission

236 electron microscopy (TEM) to elucidate the fine structure of photoreceptor synaptic regions. *Kdm3b*
237 deficiency did not affect the length of ribbon synapses of both rods and cones (Extended Data Fig. 7a). The
238 number and diameter of synaptic vesicles in the presynaptic regions of rod spherules and cone pedicles
239 showed no differences between 12-month-old *Kdm3b*^{+/+} and *Kdm3b*^{+/-} retinas (Fig. 5b and Extended Data
240 Fig. 7b). However, the mean number of docked vesicles of cone ribbon synapses decreased in 12-month-
241 old *Kdm3b*^{+/-} retinas (3.8 ± 0.35 versus 2.9 ± 0.27 , $P = 0.0285$) (Fig. 5c). These findings show that KDM3B
242 is required for the synaptic components and the visual acuity associated with cone photoreceptors.

243

244 **Electrophysiological synaptic impairment of cone photoreceptors in *Kdm3b*^{+/-} mouse retinas.** To
245 investigate the physiological role of KDM3B *in vivo*, we compared electroretinograms (ERGs) of 3-, 6- and
246 12-month-old *Kdm3b*^{+/+} and *Kdm3b*^{+/-} mice under dark-adapted (scotopic) and light-adapted (photopic)
247 conditions. The amplitude of the scotopic ERG a-wave and b-wave reflects phototransduction in the OS of
248 rods and rod bipolar cells and that of photopic ERGs, reflects both phototransduction in the OS of cones
249 and cone bipolar cell activity²¹. Under scotopic conditions, the amplitude of a-waves and b-waves, as well
250 as rod-mediated outer retinal activity were comparable between 3-, 6-, and 12-month-old *Kdm3b*^{+/+} and
251 *Kdm3b*^{+/-} mice, indicating that rod function was not significantly affected (Fig. 5d-f, and Extended Data
252 Fig. 7c-e). Under photopic conditions, the a-wave amplitude was not significantly different at both low and
253 high stimuli in 3-, 6-, and 12-month-old mouse retinas (Fig. 5g, h and Extended Data Fig. 7f-h). However,
254 photopic b-waves were significantly reduced in 6-month-old *Kdm3b*^{+/-} mice compared to those in *Kdm3b*^{+/+}
255 mice at higher stimulus luminance (194 ± 43.8 versus 129.6 ± 41.9 μV at $1.2 \log\cdot\text{cd sec/m}^2$, $P = 0.0079$),
256 which may be attributable to the impaired synaptic transmission between cones and bipolar cells (Fig. 5i
257 and Extended Data Fig. 7i). These results suggest that synapse transmission from cone photoreceptors to
258 cone bipolar cells was impaired in 6-month-old *Kdm3b*^{+/-} mice.

259

260 **Site-specific regulation of H3K9 methylation patterns by KDM3B in mouse retinas.** Because KDM3B

261 is required for the physiological and functional roles of cones, we performed ChIP-seq analysis to determine
262 whether KDM3B was directly involved in gene expression via histone demethylase activity. Over 32
263 million reads were obtained for KDM3B ChIP-seq; these were aligned with the mouse reference genome
264 (GRCm 38.99), and peak calling was performed (Supplementary Table 5). The majority of KDM3B peaks
265 were globally found within 100 Kb from the transcription start site (TSS) (Fig. 6a). The distribution of
266 KDM3B-binding peaks signified that the majority of KDM3B was localized in intergenic regions (50%)
267 and introns (42%) (Fig. 6b). To further test the functional importance of KDM3B in gene expression
268 regulation, we performed the GO analysis of the KDM3B-binding peaks. Interestingly, the KDM3B ChIP-
269 seq signals were highly enriched for genes involved in nervous system development, such as synapse
270 assembly and organization, neuron generation, and differentiation (Fig. 6c and Supplementary Table 6).

271 Previous studies have determined that KDM3B has demethylase activity for H3K9me1 and
272 H3K9me2 but not for H3K9me3^{9,22}. To determine whether KDM3B associated with H3K9me1, H3K9me2,
273 and H3K9me3 marks the same target genes, we performed H3K9me1, H3K9me2, and H3K9me3 ChIP-seq
274 using 2-month-old *Kdm3b*^{+/+} and *Kdm3b*^{+/-} mouse retinas. Similar to the results of KDM3B enrichment, the
275 majority of H3K9me1, H3K9me2, and H3K9me3 peaks were globally found within 100 Kb from the TSS,
276 and most H3K9me1, H3K9me2, and H3K9me3 peaks were localized in intergenic regions and introns
277 (Extended Data Fig. 8a, b). Consistent with the results of previous reports^{9,22}, KDM3B haploinsufficiency
278 resulted in a dramatic increase in H3K9me1 and H3K9me2 levels, while the global patterns of H3K9me3
279 levels were not significantly different between *Kdm3b*^{+/+} and *Kdm3b*^{+/-} mouse retinas (Fig. 6d). Next, all
280 H3K9me1, H3K9me2 and H3K9me3 peaks were categorized into three clusters: present in both *Kdm3b*^{+/-}
281 and *Kdm3b*^{+/+} mice (cluster 1), present only in *Kdm3b*^{+/-} mice (cluster 2), and present only in *Kdm3b*^{+/+}
282 mice (cluster 3). Centralization of ChIP-seq peaks indicated that H3K9me2 levels in cluster 2 increased
283 only in *Kdm3b*^{+/-} retinas, indicating that H3K9me2 levels are regulated in a KDM3B activity-dependent
284 manner. Also, the enrichment of H3K9me2 in cluster 3 proceeded as a demethylase-independent function
285 of KDM3B (Fig 6e). The scatter-density plot of the H3K9me2 level at the TSS between *Kdm3b*^{+/+} and

286 *Kdm3b*^{+/-} mouse retinas revealed a markedly negative correlation (Fig. 6f). Furthermore, using GO analysis,
287 we found that the H3K9me2 enriched target genes in *Kdm3b*^{+/-} retinas (cluster 2), indicating that repressed
288 genes are involved in synaptic signaling, synapse organization, and chemical synaptic transmission (Fig.
289 6g). On the other hand, the H3K9me2 peaks in *Kdm3b*^{+/+} (cluster 3) were enriched for negative regulation
290 of apoptosis and signal transduction (Fig. 6g). We obtained similar results for the global pattern of
291 H3K9me1 peaks and biological processes by GO analysis (Fig. 6h-j). Together, these ChIP-seq analyses
292 demonstrated that KDM3B is associated with H3K9me1 and H3K9me2, suggesting that KDM3B
293 exclusively regulates gene sets between neuronal homeostatic genes (synaptic transmission, vesicle
294 transport) and cell-death related genes.

295

296 **KDM3B upregulates the expression of synaptic genes through the erasure of H3K9me1 and**
297 **H3K9me2 signatures.** The balance between histone methylation and demethylation is highly correlated
298 with transcriptional regulation. We determined the molecular mechanism by which KDM3B reduced the
299 stimulation of synapse assembly genes in *Kdm3b*^{+/-} mice by integrating ChIP-seq and RNA-sequencing
300 analysis. Approximately 31% (569 genes) and 43% (803 genes) of upregulated or downregulated DEGs,
301 respectively, overlapped with all KDM3B ChIP-seq peaks (Fig. 7a, b). Consistent with RNA-sequencing
302 analysis, GO analysis showed that genes bound by KDM3B and upregulated genes were involved in DNA
303 damage stimuli and transcription regulation, while downregulated genes in *Kdm3b*^{+/-} mice were exclusively
304 enriched for neuronal development, synapse assembly, and vesicle-mediated transport (Fig. 7c-f and
305 Supplementary Table 7). We next focused on the 803 downregulated genes in *Kdm3b*^{+/-} mice to determine
306 whether gene expression was modulated by the histone demethylation activity of KDM3B. H3K9me1 and
307 H3K9me2 levels were significantly increased in association with downregulated genes in *Kdm3b*^{+/-} mice,
308 revealing the deposition of histone methylation due to the ablation of KDM3B enzymatic functions (Fig.
309 7g). Additionally, H3K9me3 level was slightly increased in some sets of downregulated genes (Fig. 7g).
310 KDM3B was enriched in the synapse assembly genes, including *Nrxn2* and *Rims2*, which were

311 downregulated in *Kdm3b*^{+/-} mice (Fig. 7h). Based on ChIP-seq data, we selected ten target genes, such as
312 synapse assembly genes and apoptosis-induced genes for validation by ChIP-qPCR. KDM3B was enriched
313 in the target gene promoters (within ~2 Kb from TSS) representing the normal range of ChIP-seq peaks for
314 H3K9me1 and H3K9me2 in *Kdm3b*^{+/+}, and the signal was significantly elevated in *Kdm3b*^{+/-} mouse retinas
315 (Fig. 7i, and Extended Data Fig. 9, 10). These results suggest that KDM3B modulated the transcriptional
316 dynamics of synaptic and apoptotic genes by balancing the H3K9 methylation status.

317

318 **KDM3B associates with AP-1 transcription factors.** Since KDM3B does not directly bind to DNA,
319 KDM3B might be associated with DNA through binding to specific transcription factors. In leukemogenesis,
320 KDM3B interacted with CBP, forming an activator complex during *lmo2* transcription activation⁹. To
321 identify potential new partners of KDM3B, we analyzed *de novo* motif discovery using the MEME-ChIP
322 algorithm. We identified a list of 10 enriched motifs (Supplementary Table 8). Two highly enriched *de novo*
323 motifs showed significant similarity to a known ZNF384 (motif enrichment E-value = 3.45e-05) and
324 transcription factor of AP-1 family (motif enrichment E-value = 1.16E-04) (JASPAR database) (Extended
325 Data Fig. 11a). Furthermore, we analyzed the positional distribution of ZNF384 and c-Jun enriched motifs
326 using the Centrimo algorithm. Both the ZNF384 and c-Jun motifs were centrally enriched with respect to
327 the KDM3B-ChIP peaks (Fig. 8a). *De novo* motif analysis of the KDM3B ChIP-seq regions yielded
328 potential binding regions for transcription factors that might co-occupy KDM3B-regulated genomic sites
329 and potentially modulate its target genes.

330 Since the AP-1 family regulates the various cellular processes, including cell proliferation,
331 differentiation, and apoptosis²³, it is reasonable to speculate that KDM3B modulates neuronal homeostatic
332 genes and cell death-related genes by interacting with AP-1 transcription factors. To test this hypothesis,
333 we first confirmed that AP-1 family (c-Fos, c-JUN, and JUNB) mRNA and protein levels were stably
334 expressed up to 12 months in mouse retina (Extended Data Fig. 11b, c). Transcriptome profiling showed
335 that *c-Fos* and *JUNB* mRNA levels increased in *Kdm3b*^{+/-} mice retina (Extended Data Fig. 11d). In addition,

336 public mRNA-sequencing data (GSE 74660) from mice retina tissue showed that the expression of *c-Fos*,
337 *c-JUN* and *JUNB* genes was higher in cone than in rod photoreceptors (Extended Data Fig. 11e). Next, we
338 analyzed whether AP-1 transcription factors were involved in KDM3B recruitment *in vivo*. Finally, co-
339 immunoprecipitation experiments showed that KDM3B was associated with c-Fos and JUNB in mice retina
340 and human lung cancer cells (Fig. 8b and Extended Data Fig. 11f). Additionally, ChIP-qPCR with c-Fos
341 and JUNB antibodies confirmed that both transcription factors were associated with KDM3B target genes
342 (Fig. 8c, and Extended Data Fig. 11g). These results suggest that KDM3B, c-Fos, and JUNB can physically
343 interact with and could regulate a set of KDM3B target genes.

344

345 ***Kdm3b* haploinsufficiency accelerated the destruction of epigenomic network robustness.** To
346 determine the difference between *Kdm3b*^{+/+} and *Kdm3b*^{+/-} networks, we constructed KDM3B-centered
347 epigenomic networks using integrated RNA-sequencing and ChIP-Seq analysis. The *Kdm3b*^{+/+} network
348 consisted of 1,452 genes with 2,906 links, while the *Kdm3b*^{+/-} network consisted of 1,376 genes with 2,384
349 links (Fig. 8d). The clustering coefficient (*Kdm3b*^{+/+} = 0.18 versus *Kdm3b*^{+/-} = 0.16) and the diameter of
350 the nodes were similar between the *Kdm3b*^{+/+} and *Kdm3b*^{+/-} networks, indicating a lack of a significant
351 difference between the global properties of the networks. To strictly measure the structural differences, the
352 network dissimilarity concept ($D(G, G')$)^{24,25} was introduced to the expanded network for four different
353 ages of *Kdm3b*^{+/+} mouse retinas (1.5, 3, 6, and 12 months) compared to those of *Kdm3b*^{+/-} mouse retinas.
354 The *D*-value among the four different ages of *Kdm3b*^{+/+} mice showed relatively small dissimilarities, from
355 0.001 to 0.012 (Fig. 8e). In contrast, there was a significant difference in the mean *D*-value between
356 *Kdm3b*^{+/+} and *Kdm3b*^{+/-} networks (0.032 ± 0.001 at 12 months) (Fig. 8e). This indicated that the network
357 dissimilarity was clear between the 12-month-old *Kdm3b*^{+/+} and *Kdm3b*^{+/-} mouse retinas.

358 Network robustness is a central question in systems biology and medicine, helping us understand
359 how subtle changes or failures lead to the development of disease²⁶. Therefore, we measured the network

360 robustness between the *Kdm3b*^{+/+} and *Kdm3b*^{+/-} genotypes by random link removal. We simulated random
361 link removal with a fraction f and measured the fraction of the largest cluster size ($P_{\infty}(f)/P_{\infty}(0)$) as an
362 order parameter (Fig. 8f). Since all epigenomic networks of KDM3B are based on centralized KDM3B
363 networks and finite-sized networks, we can predict that the critical threshold f_c goes to 1²⁷. Therefore, we
364 focused on the difference of $P_{\infty}(f)/P_{\infty}(0)$ for various values of f . The order parameters of all four
365 *Kdm3b*^{+/+} network stages showed more robustness for link failure than those of *Kdm3b*^{+/-} (Fig. 8f). These
366 results imply that the *Kdm3b* haploinsufficiency causes epigenomic network dissimilarity, resulting in the
367 acceleration of the destruction of network robustness.

368 **DISCUSSION**

369 Aging is a complex multifactorial biological process shared by all Metazoa. Organismal aging holds
370 significance for human health because it increases susceptibility to many diseases, including cancer,
371 diabetes, cardiovascular disorders, and neurodegenerative diseases. Environmental factors are the major
372 effectors that increase or decrease life expectancy. Environmental conditions may affect the cellular and
373 molecular epigenomic modifications including “loss of heterochromatin” to regulate gene expression and
374 cell fate, which result in the aggravation or alleviation of the aging process.

375 Retinal aging is often associated with a decrease in visual acuity, ocular accommodation, and dark
376 adaptation. Additionally, this aging phenotype is aggravated by several diseases, such as AMD. Recently,
377 many researchers have investigated epigenetic changes, including DNA methylation and histone
378 modification in retinal homeostasis. During the development of the vertebrate retina, multipotent
379 progenitors differentiate into various neuronal subtypes as a result of gene expression regulation^{28,29}. For
380 retinal development, the appropriate regulation of histone methylation is important for cell proliferation
381 and differentiation⁷. Histone H3K9 methyl transferase G9a (Ehmt2), mainly present in retinal progenitor
382 cells, plays an essential role in proper retinal development by repressing the expression of progenitor genes
383 in terminal differentiation³⁰. Kdm6b, which encodes H3K27 demethylase (JMJD3), is required for the
384 survival of rod bipolar cells with the regulation of Bhlhb4 expression³¹. Histone demethylase Kdm5b,
385 known as histone H3K4 demethylase, functions as a regulatory factor for rod-specific genes in the retina³².
386 Our study demonstrated that KDM3B is a putative regulator of apoptotic signaling and synaptic
387 transmission, playing a balancing role in the retinal aging process. Moreover, instead of global
388 heterochromatin loss, we found that KDM3B selectively modulates the heterochromatin features in a gene-
389 function dependent manner, i.e., differently for apoptotic or neuro-functional genes. The synapses were also
390 altered in cellular morphology and structure by downregulation of *Kdm3b* expression, indicating that
391 *Kdm3b* haploinsufficiency disturbs retinal homeostasis. Screening the expression of apoptosis-related
392 proteins in *Kdm3b*^{+/-} mice retinas revealed the upregulation of pro-apoptotic protein Bad and the

393 downregulation of anti-apoptotic protein Catalase (Fig.4e). Bad is a member of the Bcl-2 family, which was
394 identified as an intersection point between promotion and inhibition of apoptosis³³. Catalase protects against
395 oxidative stress-induced toxicity³⁴. Finally, dysregulated retinal homeostasis induces damage to cone
396 photoreceptors and initiates cell death in *Kdm3b*^{+/-} mouse retinas.

397 AMD is characterized by reduced retinal pigment epithelium (RPE) function and photoreceptor
398 loss in the macular area. Genetic variant studies of AMD can help uncover disease mechanisms and provide
399 entry points into its therapy. Despite genetic studies investigating AMD, there is a limited understanding of
400 the underlying physiological and molecular pathogenetic mechanisms and therapies of this complex disease.
401 AMD pathogenesis is triggered by genetic and environmental factors³⁵. In particular, epigenetic alteration
402 is an important factor for gene regulation without genetic variation. Of the environmental risk factors that
403 have been investigated, smoking may be associated with a two-fold increased risk of developing AMD³⁶.
404 Therefore, the integration between genetic and epigenomic studies may contribute to more effective
405 functional analyses of the mechanisms underlying AMD pathogenesis. Previous evidence supports the role
406 of aberrant epigenetic modifications with significant increase in the mRNA expression of HDAC1, HDAC3,
407 HDAC6, DNMT1, and DNMT3a in the RPE cells of mice with excessive iron levels, which are, thus, at a
408 higher risk of developing AMD³⁷. A recent study showed *KDM3B* SNPs caused eye abnormalities (31%,
409 5/16 cases), such as nystagmus and strabismus in four individuals, as well as refraction anomalies and low
410 vision in three individuals³⁸. We generated heterozygous *Kdm3b* mice and focused on the function of
411 KDM3B in the mouse retina via physiological, genetic, and multi-dimensional epigenomic analysis. We
412 found that *Kdm3b* mRNA expression is similar between rods and cones during development, but the protein
413 level is highly enriched only in cones (Extended Data Fig. 3). Thus, KDM3B has cell type specificity and
414 different functional roles at the protein level. ONL thickness and cone photoreceptor populations can be
415 reduced in *Kdm3b*^{+/-} mouse retina by regulating apoptotic genes (Fig. 2 and 4). Furthermore, KDM3B plays
416 an important role in synapse assembly and vesicle transport in cone ribbon synapses through multi-
417 dimensional epigenomic network analysis (Fig. 8d-f). We suggest that the cone-cell type specificity and

418 KDM3B functional network can cause age-related diseases, such as AMD. Future studies will demonstrate
419 whether KDM3B is associated with cone-cell type specificity in the human retina.

420 The duplex retina in vertebrates constitutes specialized light-sensitive rod and cone
421 photoreceptors³⁹. Rods permit energy conservation and maximum sensitivity at the expense of spatial and
422 temporal resolution, whereas cones enable non-quenching, rapid responses to photons with high acuity in
423 daylight⁴⁰. Rods and cones coordinate synaptic connections with bipolar and horizontal cells for visual
424 transmission. Previous studies have shown the important roles of epigenetic regulation in retinal
425 development and homeostatic maintenance. For instance, the histone H3K4 methyl transferase MLL1, is
426 essential for retinal structure, functional synapse formation, horizontal cell differentiation, and
427 maintenance⁴¹. Ablation BMI1, a component of the PRC1 histone H3K27 methyl transferase complex, leads
428 to increased retinal cell death in bipolar and cone cells⁴². Despite these observations, the exact role of
429 epigenetic regulation in photoreceptor development and degeneration is largely unknown. We demonstrated
430 the functional morphology and physiology of cone synapses in the *Kdm3b*^{+/-} retina. Reduced ERG waves
431 in *Kdm3b*^{+/-} mice imply defective phototransduction in cones. A higher decrease in B-waves than in A-
432 waves in photopic ERGs suggests abnormalities in visual transmission in cones. The number of cone ribbon
433 synapses and docked vesicles in cone pedicles were reduced in *Kdm3b*^{+/-} mice (Fig. 5). Additionally,
434 *Kdm3b*^{+/-} mouse retinas showed that the synapse assembly genes including *Rims2*, *Nrxn2*, *CtBP2*, *Nedd4*,
435 and vesicle-transport genes, including *Tmed10*, *Vamp4* were downregulated by increasing H3K9
436 methylation (Fig. 7). This suggests that the presynaptic terminal abnormalities in cones proceed from
437 epigenetic modification complications followed by incorrect assembly of ribbon synapses.

438 Rising evidence suggested that epigenetic modulators often exhibit dual function, both activator
439 and repressor, in gene transcriptional regulation, development, and cancer progression. However, how these
440 dual functions are coordinated in specific cellular contexts remains poorly understood. Therefore, it is
441 interesting that KDM3B, an active histone demethylase, unexpectedly activates apoptotic genes in aged
442 *Kdm3b*^{+/-} mice retinas. Since KDM3B lacks DNA binding ability, it may require a transcription factor for

443 gene-set specific regulation. Consistent with this hypothesis, our RNA-sequencing analysis supported an
444 increasing expression pattern of AP-1 family transcription factors during retinal aging. In addition, motif
445 analysis of KDM3B ChIP-seq data uncovered a list of transcription factors that were associated with
446 specific target genes. In particular, KDM3B peaks carried a motif predicted by AP-1 family transcription
447 factors such as c-Fos and JUNB. We demonstrated that KDM3B co-occupies a subset of KDM3B target
448 genes via physical interaction; however, it remains to be determined if this interaction is direct or indirect
449 (Fig. 8). The immediate early gene *c-Fos* is expressed in various cell types by numerous stimuli and
450 conditions. C-Fos is well known to dimerize with c-JUN family proteins, which are a major component of
451 the AP-1 transcriptional complex. Previous reports indicate that c-Fos is implicated in the induction of cell
452 death in several types of neuronal cells. c-Fos is required for both regeneration of retina ganglion cells and
453 apoptotic cell death^{43,44}. Consistent with the results from previous studies, we observed that c-Fos and JUNB
454 are associated with KDM3B at the regulatory regions of apoptosis-induced genes and synapse assembly
455 genes in mice retina. This finding further supports the assertion that c-Fos and JUNB might fine-tune the
456 transcription of KDM3B target genes acting as on-off switches during aging. Although detailed mechanisms
457 are yet to be elucidated, our data shed some light on novel aging regulatory mechanisms.

458 GRNs affect all biological phenomena associated with maturation (development), rapid
459 destruction (disease), and slow destruction (aging) (Fig. 8g). In terms of network topology, conventional
460 GRNs cannot differentiate between subtle changes, such as environmental adverse effects and aging. We
461 suggest that the integration of multi-dimensional epigenomic networks and GRNs will help improve the
462 understanding of biological phenomena by allowing for the measurement of network strength during aging.
463 We focused on an epigenetic regulator (KDM3B)-centered network during retinal aging. Even though many
464 studies have investigated epigenetic regulation in cancers or stem cells, the precise mechanism of
465 epigenomic modification in completely differentiated and aging cells is largely unknown. KDM3B is an
466 H3K9me1 and H3K9me2 demethylase that belongs to the KDM3 family and acts as a transcriptional
467 activator^{9,45}. KDM3B accelerates leukemogenesis by regulating *lmo2* expression via the reduction of

468 H3K9me2 methylation²². Additionally, the demethylation activity of KDM3A/B activates Wnt target genes,
469 which increase the survival of human colorectal cancer stem cells²². Previous reports implicate H3K9
470 methylation remodeling in aging. Histone methyl transferase SUV39H1 decreases in line with age, resulting
471 in a reduction of global H3K9me level and disturbed heterochromatin function⁴⁶. Another report showed
472 that the disruption of Kdm4A causes shortening of the lifespan of male *Drosophila*, indicating that KDM4A
473 is involved in longevity⁴⁷. We established *Kdm3b*^{+/-} mice and demonstrated the functional roles of KDM3B
474 via morphological and physiological changes, as well as genome-wide transcriptional and epigenomic
475 analysis during retinal aging. Importantly, our data suggest that site-specific changes of H3K9 methylation
476 in *Kdm3b*^{+/-} mice accelerate the destruction of GRN leading to “loss of heterochromatin features” affecting
477 cellular lifespan depending on organism. Furthermore, we constructed the KDM3B-centered GRN using
478 integrated RNA-Sequencing and ChIP-Seq analysis, which showed that the strength of the network between
479 a transcriptional regulator and its target genes weakened in *Kdm3b*^{+/-} mice. Although the network structural
480 properties are not significantly different between *Kdm3b*^{+/+} and *Kdm3b*^{+/-} mice (Fig. 8d), we found interior
481 topological differences by measuring network dissimilarity and robustness (Fig. 8f). Eventually, *Kdm3b*
482 haploinsufficiency diminished the structural gene network via heterochromatin misregulation and induced
483 cascading destruction of network integrity; these delicate alterations emerged as post-transcriptional and
484 translational regulations. For example, disrupted alternative splicing of the *CPSF1* and *CNOT3* genes leads
485 to the attenuation of biological processes in retinitis pigmentosa (RP)⁴⁸. We identified the retained intron
486 events on the *Aldoa* gene in *Kdm3b*^{+/-} mouse retinas (Extended Data Fig. 5d). ALDOA is a glycolytic
487 enzyme that catalyzes the reversible conversion of fructose-1, 6-bisphosphate to glyceraldehyde 3-
488 phosphate and dihydroxyacetone phosphate⁴⁹. This result suggests that *Kdm3b* haploinsufficiency changes
489 the normal transcriptome profile, which is a potential cause of retinal disease via energy metabolism
490 regulation during aging.

491 In summary, our findings provide new insight into how site-specific epigenetic regulation
492 contributes to the maintenance of retinal homeostasis during aging. We demonstrated the presence of an

493 epigenomic network in the retina, which might illuminate the selective roles of KDM3B in synaptic
494 transmission and apoptotic signaling pathways during retinal aging. We integrated epigenomic network
495 analysis with physiological and morphological analyses of the *Kdm3b*^{+/-} mouse retina. Ablation of *Kdm3b*
496 results in presynaptic cone abnormalities by inducing apoptotic signals. *Kdm3b* haploinsufficiency
497 downregulates a subset of synapse assembly genes, with H3K9 methylation-associated silencing. Overall,
498 these findings suggest that integrating genomic and epigenomic data in network studies can help to predict
499 whether subtle changes in network strength increase susceptibility to age-related neuronal disease.

500 **METHODS**

501 **Animals.** *Kdm3b*^{+/-} mice were developed by a gene trapping system using pGT01xf plasmid inserted
502 between exons 12 and 13 of the *Kdm3b* gene. *Kdm3b*^{+/-} genotype was confirmed by PCR using genotyping
503 primers: common forward, 5'-GGC ACC AGA CCC TGG GAG CTA G-3'; WT reverse, 5'-CAC CCA
504 CGA CCT GGC TTA CAC C-3'; and KO reverse 5'-CAC CCA CGA CCT GGC TTA CAC C-3'. Mice
505 were maintained in a 12-h light-dark cycle (lights were turned off at 20:00) with free access to water and
506 mouse feed. The mice were weaned at the age of 3 weeks and housed 1-6 per cage. Mice were approved by
507 the Institutional Review Board of Chung-Ang University (updated IRB number: 2019-00059 and 2020-
508 00061).

509

510 **Immunohistochemistry (IHC).** *Kdm3b*^{+/-} mice retinas were excised quickly by removing the lenses on a
511 cold plate submerged in PBS. After fixation of retinal tissues with 4% paraformaldehyde (#15710; Electron
512 Microscopy Sciences, Hatfield, PA, USA), they were incubated successively in 10%, 20%, 30% sucrose-
513 PBS for 1, 3, and 12 h, each. The fixed retina was embedded with 7% agarose gel or OCT compound (4583,
514 SAKURA, CA, USA), and the retinas were sectioned with vibratome (7000SMZ, Campden Instruments,
515 England) and cryotome (CM1850, Leica, Germany). After permeabilization in PBS with 0.1% Triton X-
516 100 for 10 min, the sections were incubated for 1 h in blocking solution, which included 5% normal goat
517 serum in PBS with 0.1% Triton X-100. Primary antibodies were incubated overnight at 4°C. Secondary
518 antibodies were incubated for 1 h at 23-25°C in the dark after being washed with PBS. The list of antibodies
519 is presented in Supplementary Table 9. The nucleus was counterstained with 5 µg/ml 40, 60-diamidino-2-
520 phenylindole (DAPI) for 3 min in the dark. Fluorescence images were generated with Zeiss Axio Observer
521 Z1 LSM 700 confocal microscope and ZEN program (ZEN lite 2011) (Carl Zeiss, Oberkochen, Germany).

522

523 **Immunoprecipitation and immunoblotting.** The retina tissues were lysed in a buffer containing 1% Triton
524 X-100, 150 mM NaCl, 50 mM Tris-HCl, pH 7.5, 0.1% sodium dodecyl sulfate (SDS), 1% Nonidet P-40,

525 and 1 mM PMSF. The cell suspensions of retina tissue were homogenized on ice and centrifuged at 15,000
526 g at 4°C for 10 min. For immunoprecipitation assays, the supernatants were precleaned with 20 µl of protein
527 A/G magnetic agarose beads (50% slurry) and then incubated at 4°C overnight with 40 µl of protein A/G
528 magnetic agarose beads in the presence of appropriate antibodies. The beads were washed 3 times in PBS,
529 resuspended in SDS sample buffer, and boiled for 10 min. The protein samples from the retina were
530 electrophoresed on a 10% SDS-PAGE and transferred to a nitrocellulose membrane (Protran™; Whatman,
531 Maidstone, UK). The membrane was blocked with 5% skim milk in TBS-T buffer (137 mM NaCl, 20 mM
532 Tris-HCl, pH 7.6 and 0.1% Tween-20) and incubated with suitable diluted primary antibody overnight at
533 4°C. The list of antibodies is presented in Supplementary Table 9. The membranes were washed thrice for
534 10 min each with TBST and incubated with a 1:5,000 dilution of horseradish peroxidase-conjugated anti-
535 mouse or anti-rabbit antibodies for 1 hr. Blots were washed with TBST three times and developed with the
536 Western blotting luminol reagent (sc-2048, Santa Cruz), according to the manufacturer's protocols.

537
538 **Total RNA isolation and RT-qPCR.** Total RNA was extracted using the TRIzol solution (15596018,
539 Invitrogen, CA, USA) according to the manufacturer's specifications. Contaminated genomic DNA was
540 removed from 10 µg of total RNA by incubation with 20 units of Rnase-free Dnase I (New England Biolabs)
541 and 4 units of RNase inhibitor (New England Biolabs) in DEPC-treated water. The reaction mix was
542 incubated for 1 hr at 37°C and then for 10 min at 50°C. RNA samples were quantified
543 spectrophotometrically at 260 nm and all RNA extracts had an OD₂₆₀:OD₂₈₀ between 1.8 and 2.0,
544 demonstrating that RNA was extracted clearly. Oligo-dT (6110A, Takara) was applied as the primer in the
545 first step of cDNA synthesis. Total RNA (1 µg) was combined with 1 µl of oligo dT and H₂O and then
546 preheated at 70°C for 10 min to denature the secondary structures of RNA. The mix was then quickly cooled
547 to 4°C, then 10 mM DTT, 2 µl of 10X reverse-transcriptase buffer, and 200 units of reverse transcriptase
548 (18064022, Invitrogen, CA, USA) were added to make a total volume of 20 µl. The reverse-transcriptase
549 mixture was incubated at 40°C for 60 min, subsequently the reaction was stopped by heating at 94°C for

550 20 s. The cDNA stock was stored at -20°C.

551 The specificity of each of the amplified products was confirmed by melting curve analysis. For real-time
552 quantitative PCR, the iQ SYBR Green PCR Supermix (#1708880, Bio-Rad) and the CFX96 Real-time PCR
553 detection system (Bio-Rad) were used to detect amplified cDNA samples according to the manufacturer's
554 instructions. The β -actin gene was used for normalization. The relative mRNA expression was calculated
555 by the $2^{-(\Delta\Delta Ct)}$ method.

556

557 **ERG analysis.** Mice were given full field flash ERG to assess retinal function under scotopic and photopic
558 conditions⁵⁰. Mice were adapted to dark overnight for scotopic measurements and anaesthetized with 2X
559 avertin solution (200 μ l per 20 g mouse) with tribromoethanol (T48402, SIGMA) and tert-amyl alcohol
560 (240486, SIGMA). Their pupils were dilated with isopto atropine (Alcon, Republic of Korea), and a small
561 drop of 1% hypromellose (Samil, Republic of Korea) was added to each eye before measurements. Ground
562 and reference subdermal electrodes were placed subcutaneously near the hindquarter and between the eyes,
563 respectively and the mice were placed on heated pads (37 °C). Recording electrodes were placed on the
564 cornea, and ERG was carried out under scotopic conditions for both eyes simultaneously, with increasing
565 green light stimulus strengths. After the mice adapted to 1.6 log cd·sec/m² for 5 min, the photopic responses
566 were recorded.

567

568 **Mouse apoptosis antibody array.** The expression of apoptosis-related proteins in mice retinas was
569 analyzed using a Mouse Apoptosis Array Kit (R&D Systems, Minneapolis, MN, USA). All procedures were
570 performed according to manufacturer's instructions. Nitrocellulose-membrane sheets containing 21
571 apoptosis-related proteins were incubated with blocking buffer at room temperature for 1 h, then the mouse
572 retina lysates were incubated overnight with the membranes at 4°C. After rinsing, the array was incubated
573 with a cocktail of biotinylated detection antibodies at room temperature for 1 hr and probed with HRP-
574 conjugated streptavidin for 30 min. A signal produced at each capture spot corresponding to the amount of

575 protein bound was detected. Relative protein levels were estimated by comparing the pixel densities of
576 protein spots and were quantified using ImageJ.

577

578 **Transmission electron microscopic (TEM) analyses.** Mice retinas were enucleated and fixed in 4%
579 paraformaldehyde overnight at 4°C. After three washes with 0.1 M sodium cacodylate buffer, pH 7.2, they
580 were fixed in 1% osmium tetroxide/0.1 M cacodylate buffer. The retinas were dehydrated using an ethanol
581 gradient up to 100%, and embedded in epoxy resin. Ultrathin sections were prepared using an ultracut
582 diamond knife and stained with 2% uranyl acetate and 4% lead citrate. Specimens were visualized with a
583 TEM (Tecnai F20 G2).

584

585 **RNA sequencing and bioinformatic analysis.** RNA-sequencing library was generated by TruSeq mRNA
586 Library Prep Kit (Illumina, Inc., USA) according to the manufacturer's instructions. Briefly, 100 ng total
587 RNA from the retinas was isolated and an oligo-dT primer including an Illumina-compatible sequence at
588 its 5' end was hybridized to the RNA and reverse transcription was carried out. After the degradation of the
589 RNA template, second strand synthesis was initiated by a random primer containing an Illumina-compatible
590 linker sequence at its 5' end. The double-stranded library was purified by employing AMPure magnetic
591 beads (A63881, Beckman coulter, CA, USA) to get rid of all reaction components. The library was
592 amplified to add the complete adapter sequences required for cluster generation. The finished library was
593 purified from PCR components. High-throughput sequencing was carried out as paired-end 75-sequencing
594 reads using NextSeq 500 (Illumina, Inc., USA). Alignment of mRNA-Sequencing reads was performed
595 using STAR-2.5.4b (Supplementary Table 10). Indices were either produced from genome assembly
596 sequence or the representative transcript sequences for aligning to the genome and transcriptome. The
597 alignment file was applied for assembling transcripts, estimating their abundances, and detecting
598 differential expression of genes. Differentially expressed transcripts were determined based on counts from
599 unique and multiple alignments using Edge R within R version 3.6.3 (R development Core Team, 2011)

600 using R package.

601

602 **Chromatin immunoprecipitation (ChIP) sequencing.** Retina tissue samples were cross-linked with 1%
603 paraformaldehyde for 10 min at 23°C and glycine (final concentration: 125 mM) was added to quench the
604 reaction. The samples were homogenized in SDS lysis buffer (1% SDS, 10 mM EDTA, and 50 mM Tris-
605 HCl, pH 8.1), and chromatin was then sheared using a bioruptor sonicator (Diagenode) for 40 cycles (30s
606 on / 30s off, repeated 2 times) at high power setting. After centrifugation for 10 min at 18,500 g, the samples
607 were resuspended in ChIP dilution buffer (0.01% SDS, 1.2 mM EDTA, 1.1% Triton X-100, 167 mM NaCl,
608 and 16.7 mM Tris-HCl, pH 8.1). The sonicated lysates were subjected to immunoprecipitation using the
609 indicated antibodies (5 µg of antibodies for each immunoprecipitation (IP) reaction) overnight. Protein A/G
610 magnetic beads (26162, Thermo scientific, USA) (30 µl) were added, and immunoprecipitations were
611 continued for an additional 4 h, and washed with low-salt wash buffer (0.1% SDS, 1% Triton X-100, 2 mM
612 EDTA, 150 mM NaCl, 20 mM Tris-HCl, pH 8.1), high-salt wash buffer (0.1% SDS, 1% Triton X-100, 2
613 mM EDTA, 500 mM NaCl, 20 mM Tris-HCl, pH 8.1), LiCl immune-wash buffer (0.25M LiCl, 1% NP40,
614 1% deoxycholate, 1 mM EDTA, 10 mM Tris-HCl, pH 8.1), and Tris-EDTA buffer (1 mM EDTA, 10 mM
615 Tris-HCl, pH 8.0). Following the final wash, the precipitates were eluted with 100 µl of IP elution buffer
616 (1% SDS, 0.1 M NaHCO₃) twice and reverse cross-linked by incubating overnight at 65°C overnight.
617 DNA/protein complexes were precipitated with 100% ethanol, air-dried, and dissolved in 20 µl of distilled
618 water (W4502, Sigma). The list of primers used for validation of ChIP-seq is described in Supplementary
619 Table 11.

620

621 **ChIP-seq library preparation and bioinformatic analysis.** ChIP-seq library was generated by TruSeq
622 ChIP Library Preparation Kit (Set A, IP-202-1012, Set B, IP-202-1024, Illumina, CA, USA) according to
623 the manufacturer's instructions. Briefly, 5 µg of input and ChIP-enriched DNA were end-repaired, A-tailed,
624 adapter ligated with TruSeq index adapters, and amplified. Paired-end sequencing of all ChIP libraries was

625 performed on the Illumina NextSeq 500 platform. For processing of KDM3B and histone modification
626 ChIP-seq in the retina, all ChIP reads in FASTQ format were aligned to the GRCm 38.99 mouse genome
627 using Bowtie2 (v2.3.4.1) and redundant reads were removed (Supplementary Table 12). Peak calling was
628 performed with EPIC2 (v0.0.41) with the default parameters: bin size = 200; fragment size = 150; Gap
629 allowed = 3, FDR cutoff < 0.05). After confirming the consistency between each replicate, we pooled
630 extended reads to generate a bigwig track for visualization with IGV (v2.8.7).

631

632 **Motif discovery.** Overrepresented motif analysis of sequences enriched under KDM3B ChIP-seq peaks
633 was performed using the de novo motif finder MEME-ChIP [<http://meme.nbcr.net/meme/tools/meme-chip>,
634 date last accessed, July 2015]. A 300-bp sequence surrounding each of the ChIP-Seq peak summits
635 (extending 150 bp on each side) was supplied to MEME-ChIP as input and analyzed with the default settings
636 for motif width and significance thresholds.

637

638 **GO and GSEA analysis.** DAVID (<http://david.abcc.ncifcrf.gov>) allowed significant DEGs and ChIP-seq
639 peaks in respective gene sets to be clustered into functional gene ontologies. Enriched gene ontology terms
640 were identified using Metascape, and scatter plots of ontology terms were made using REVIGO⁵¹. GSEA
641 analysis was performed using (GSEA 4.1.0; <http://www.broadinstitute.org/gsea/index.jsp>) the MsigDB v7.1
642 mouse database.

643

644 **Epigenomic network construction.** KDM3B-centered network was constructed by integrating RNA-
645 sequencing and ChIP-Seq data analysis as follows: First, the nearest neighbor (NN) genes for KDM3B were
646 selected by filtering condition (ChIP-count > 10 per each gene). Next, 2nd NN genes of KDM3B were
647 identified using NetworkAnalyst⁵². The selected 2nd NN gene was linked with the 1st NN gene. All networks
648 were considered by the 3rd NN. For all candidate genes of a network, genes from RNA-sequencing were
649 filtered using FPKM > 10. For measurement of network robustness, we compared the impact of random

650 link removal on the KDM3B-centered networks between *Kdm3b*^{+/+} (1.5, 3, 6, and 12 months) and *Kdm3b*^{+/-}
651 (12 months) mice.

652

653 **Measurement of network structural dissimilarities.** Network dissimilarity measurement was done
654 following the approach proposed by Shieber et al.²⁴. This method compared network structures based on
655 quantifying differences among distance distributions, node dispersion metric, and α -centrality.

$$656 \quad D(G, G') = w_1 \sqrt{\frac{I(\mu_G, \mu_{G'})}{\log 2}} + w_2 \left| \sqrt{NND(G)} - \sqrt{NND(G')} \right| + \frac{w_3}{2} \left(\sqrt{\frac{J(P_{\alpha G}, P_{\alpha G'})}{\log 2}} + \sqrt{\frac{J(P_{\alpha G^c}, P_{\alpha G'^c})}{\log 2}} \right)$$

657 Here, J represents Jensen-Shannon divergence. The first term represents dissimilarity in average node
658 connectivity μ_G is the graphs averaged node-distance distribution. The second term shows dissimilarity in
659 a node dispersion metric ($NND(G)$). And the last term denotes the difference for distribution of α -
660 centrality ($P_{\alpha G}, P_{\alpha G'^c}$) that measures the influence of a node in the given graph G and its complement
661 graph (G^c). We measured network dissimilarity following the algorithm²⁴, using $w_1 = 0.45$, $w_2 = 0.45$, $w_3 =$
662 0.1 values.

663

664 **Image analysis.** The number of nuclei in ONL was counted on the middle of the *Kdm3b*^{+/+} and *Kdm3b*^{+/-}
665 mice retina. The thickness of ONL was measured using the ‘length measurement’ plugin of ImageJ software.
666 The number of cone photoreceptors was counted in the middle of *Kdm3b*^{+/-} mouse inferior retina. Size of
667 cone photoreceptor synapse was measured by using the ‘area measurement’ plugin of ImageJ software.
668 Intensities of GFAP and cytochrome c were measured using the ‘histogram’ plugin of ImageJ software. The
669 3D reconstruction image was generated using Oxford Bitplane Imaris (v9.3.1, Bitplane, CT, USA)

670

671 **Statistical analysis.** Student’s t -test was used to examine the significance of differences between data with
672 GraphPad PRISM. The results are denoted as mean \pm standard error of the mean (SEM), which are obtained

673 from two or three separated experiments. *P* values less than 0.05 were considered statistically significant.

674

675 **Data availability.** RNA-sequencing and ChIP-seq data that support the findings of this study have been

676 deposited in NCBI GenBank with the primary accession code GSE160793. All other data are present in the

677 article and its Supplementary files, or are available from the corresponding author upon reasonable request.

678 Source data are provided with this paper. Recheck and GEO confirm.

679 **REFERENCES**

- 680 1. Levin, O., Fujiyama, H., Boisgontier, M.P., Swinnen, S.P. & Summers, J.J. Aging and motor
681 inhibition: a converging perspective provided by brain stimulation and imaging approaches.
682 *Neurosci Biobehav Rev* **43**, 100-117 (2014).
- 683 2. Campello, L. *et al.* Aging of the Retina: Molecular and Metabolic Turbulences and Potential
684 Interventions. *Annu Rev Vis Sci* **7**, 633-664 (2021).
- 685 3. Saul, D. & Kosinsky, R.L. Epigenetics of Aging and Aging-Associated Diseases. *Int J Mol Sci*
686 **22**(2021).
- 687 4. Nicetto, D. & Zaret, K.S. Role of H3K9me3 heterochromatin in cell identity establishment and
688 maintenance. *Curr Opin Genet Dev* **55**, 1-10 (2019).
- 689 5. Keenan, C.R. *et al.* Extreme disruption of heterochromatin is required for accelerated
690 hematopoietic aging. *Blood* **135**, 2049-2058 (2020).
- 691 6. Ito, T., Teo, Y.V., Evans, S.A., Neretti, N. & Sedivy, J.M. Regulation of Cellular Senescence by
692 Polycomb Chromatin Modifiers through Distinct DNA Damage- and Histone Methylation-
693 Dependent Pathways. *Cell Rep* **22**, 3480-3492 (2018).
- 694 7. Corso-Diaz, X., Jaeger, C., Chaitankar, V. & Swaroop, A. Epigenetic control of gene regulation
695 during development and disease: A view from the retina. *Prog Retin Eye Res* **65**, 1-27 (2018).
- 696 8. Mosammaparast, N. & Shi, Y. Reversal of histone methylation: biochemical and molecular
697 mechanisms of histone demethylases. *Annu Rev Biochem* **79**, 155-79 (2010).
- 698 9. Kim, J.Y. *et al.* KDM3B is the H3K9 demethylase involved in transcriptional activation of lmo2 in
699 leukemia. *Mol Cell Biol* **32**, 2917-33 (2012).
- 700 10. Yamane, K. *et al.* JHDM2A, a JmjC-containing H3K9 demethylase, facilitates transcription
701 activation by androgen receptor. *Cell* **125**, 483-95 (2006).
- 702 11. An, M.J. *et al.* Histone demethylase KDM3B regulates the transcriptional network of cell-cycle
703 genes in hepatocarcinoma HepG2 cells. *Biochem Biophys Res Commun* **508**, 576-582 (2019).
- 704 12. Peter, I.S. & Davidson, E.H. Evolution of gene regulatory networks controlling body plan
705 development. *Cell* **144**, 970-85 (2011).
- 706 13. Davidson, E.H. & Levine, M.S. Properties of developmental gene regulatory networks. *Proc Natl*
707 *Acad Sci U S A* **105**, 20063-6 (2008).
- 708 14. Kim, J.W. *et al.* NRL-Regulated Transcriptome Dynamics of Developing Rod Photoreceptors. *Cell*
709 *Rep* **17**, 2460-2473 (2016).
- 710 15. Poleshko, A. *et al.* H3K9me2 orchestrates inheritance of spatial positioning of peripheral
711 heterochromatin through mitosis. *Elife* **8**(2019).

- 712 16. Zhang, T., Cooper, S. & Brockdorff, N. The interplay of histone modifications - writers that read.
713 *EMBO Rep* **16**, 1467-81 (2015).
- 714 17. Kim, Y.G. *et al.* Kdm3b haploinsufficiency impairs the consolidation of cerebellum-dependent
715 motor memory in mice. *Mol Brain* **14**, 106 (2021).
- 716 18. Cepko, C.L. The roles of intrinsic and extrinsic cues and bHLH genes in the determination of retinal
717 cell fates. *Curr Opin Neurobiol* **9**, 37-46 (1999).
- 718 19. Abler, A.S., Chang, C.J., Ful, J., Tso, M.O. & Lam, T.T. Photic injury triggers apoptosis of
719 photoreceptor cells. *Res Commun Mol Pathol Pharmacol* **92**, 177-89 (1996).
- 720 20. Baden, T., Euler, T., Weckstrom, M. & Lagnado, L. Spikes and ribbon synapses in early vision.
721 *Trends Neurosci* **36**, 480-8 (2013).
- 722 21. Sharma, S., Ball, S.L. & Peachey, N.S. Pharmacological studies of the mouse cone
723 electroretinogram. *Vis Neurosci* **22**, 631-6 (2005).
- 724 22. Li, J. *et al.* KDM3 epigenetically controls tumorigenic potentials of human colorectal cancer stem
725 cells through Wnt/beta-catenin signalling. *Nat Commun* **8**, 15146 (2017).
- 726 23. Shaulian, E. & Karin, M. AP-1 as a regulator of cell life and death. *Nat Cell Biol* **4**, E131-6 (2002).
- 727 24. Schieber, T.A. *et al.* Quantification of network structural dissimilarities. *Nat Commun* **8**, 13928
728 (2017).
- 729 25. Dehmer, M. & Emmert-Streib, F. Comments to “Quantification of network structural dissimilarities”
730 published by Schieber *et al.* *Mathematical Methods in the Applied Sciences* **41**, 5711-5713 (2018).
- 731 26. Barabási, A.-L. *Network science*, (Cambridge university press, 2016).
- 732 27. Cohen, R., Erez, K., ben-Avraham, D. & Havlin, S. Resilience of the internet to random
733 breakdowns. *Phys Rev Lett* **85**, 4626-8 (2000).
- 734 28. Swaroop, A., Kim, D. & Forrest, D. Transcriptional regulation of photoreceptor development and
735 homeostasis in the mammalian retina. *Nat Rev Neurosci* **11**, 563-76 (2010).
- 736 29. Iwagawa, T. & Watanabe, S. Molecular mechanisms of H3K27me3 and H3K4me3 in retinal
737 development. *Neurosci Res* **138**, 43-48 (2019).
- 738 30. Katoh, K., Yamazaki, R., Onishi, A., Sanuki, R. & Furukawa, T. G9a histone methyltransferase
739 activity in retinal progenitors is essential for proper differentiation and survival of mouse retinal
740 cells. *J Neurosci* **32**, 17658-70 (2012).
- 741 31. Iida, A. *et al.* Histone demethylase Jmjd3 is required for the development of subsets of retinal
742 bipolar cells. *Proc Natl Acad Sci U S A* **111**, 3751-6 (2014).
- 743 32. Hao, H. *et al.* Transcriptional regulation of rod photoreceptor homeostasis revealed by in vivo NRL
744 targetome analysis. *PLoS Genet* **8**, e1002649 (2012).

- 745 33. Kale, J., Osterlund, E.J. & Andrews, D.W. BCL-2 family proteins: changing partners in the dance
746 towards death. *Cell Death Differ* **25**, 65-80 (2018).
- 747 34. Bai, J. & Cederbaum, A.I. Mitochondrial catalase and oxidative injury. *Biol Signals Recept* **10**, 189-
748 99 (2001).
- 749 35. Sobrin, L. & Seddon, J.M. Nature and nurture- genes and environment- predict onset and
750 progression of macular degeneration. *Prog Retin Eye Res* **40**, 1-15 (2014).
- 751 36. Smith, W. *et al.* Risk factors for age-related macular degeneration: Pooled findings from three
752 continents. *Ophthalmology* **108**, 697-704 (2001).
- 753 37. Gnana-Prakasam, J.P. *et al.* Loss of Hfe leads to progression of tumor phenotype in primary retinal
754 pigment epithelial cells. *Invest Ophthalmol Vis Sci* **54**, 63-71 (2013).
- 755 38. Diets, I.J. *et al.* De Novo and Inherited Pathogenic Variants in KDM3B Cause Intellectual Disability,
756 Short Stature, and Facial Dysmorphism. *Am J Hum Genet* **104**, 758-766 (2019).
- 757 39. Lin, L., Wang, W., Du, C. & Luo, X. A cone-shaped concentrator with varying performances of
758 concentrating. *Opt Express* **16**, 6809-14 (2008).
- 759 40. Sharpe, L.T., Stockman, A., Jagle, H., Knau, H. & Nathans, J. L, M and L-M hybrid cone
760 photopigments in man: deriving lambda max from flicker photometric spectral sensitivities. *Vision*
761 *Res* **39**, 3513-25 (1999).
- 762 41. Brightman, D.S. *et al.* MLL1 is essential for retinal neurogenesis and horizontal inner neuron
763 integrity. *Sci Rep* **8**, 11902 (2018).
- 764 42. Barabino, A. *et al.* Loss of Bmi1 causes anomalies in retinal development and degeneration of cone
765 photoreceptors. *Development* **143**, 1571-84 (2016).
- 766 43. Curran, T. & Morgan, J.I. Fos: an immediate-early transcription factor in neurons. *J Neurobiol* **26**,
767 403-12 (1995).
- 768 44. Oshitari, T. *et al.* The role of c-fos in cell death and regeneration of retinal ganglion cells. *Invest*
769 *Ophthalmol Vis Sci* **43**, 2442-9 (2002).
- 770 45. Krieg, A.J. *et al.* Regulation of the histone demethylase JMJD1A by hypoxia-inducible factor 1
771 alpha enhances hypoxic gene expression and tumor growth. *Mol Cell Biol* **30**, 344-53 (2010).
- 772 46. Djeghloul, D. *et al.* Age-Associated Decrease of the Histone Methyltransferase SUV39H1 in HSC
773 Perturbs Heterochromatin and B Lymphoid Differentiation. *Stem Cell Reports* **6**, 970-984 (2016).
- 774 47. Lorbeck, M.T. *et al.* The histone demethylase Dmel\Kdm4A controls genes required for life span
775 and male-specific sex determination in Drosophila. *Gene* **450**, 8-17 (2010).
- 776 48. Buskin, A. *et al.* Disrupted alternative splicing for genes implicated in splicing and ciliogenesis
777 causes PRPF31 retinitis pigmentosa. *Nat Commun* **9**, 4234 (2018).

- 778 49. Du, S. *et al.* Fructose-bisphosphate aldolase a is a potential metastasis-associated marker of lung
779 squamous cell carcinoma and promotes lung cell tumorigenesis and migration. *PLoS One* **9**, e85804
780 (2014).
- 781 50. Hoh Kam, J., Lenassi, E., Malik, T.H., Pickering, M.C. & Jeffery, G. Complement component C3
782 plays a critical role in protecting the aging retina in a murine model of age-related macular
783 degeneration. *Am J Pathol* **183**, 480-92 (2013).
- 784 51. Zhou, Y. *et al.* Metascape provides a biologist-oriented resource for the analysis of systems-level
785 datasets. *Nat Commun* **10**, 1523 (2019).
- 786 52. Zhou, G. *et al.* NetworkAnalyst 3.0: a visual analytics platform for comprehensive gene expression
787 profiling and meta-analysis. *Nucleic Acids Res* **47**, W234-W241 (2019).

788 **ACKNOWLEDGEMENTS**

789 The study was supported by the Korean Environment Industry & Technology Institute (KEITI) through
790 “The Environmental Health Action Program” (Grant and Award number: 2017001360007) and “Digital
791 Infrastructure Building Project for Monitoring, Surveying and Evaluating the Environmental Health
792 Program” (Grant and Award number: 2021003330007) funded by the Korean Ministry of Environment
793 (MOE). This work was also supported by the National Research Foundation of Korea (NRF) grant funded
794 by the Korean government (MIST) (Basic Research Laboratory: NRF-2019R1A4A2001609; NRF-
795 2018R1D1A1B07050755). *Kdm3b* heterozygous mouse was kindly gifted by Prof. Sang-Beom Seo
796 (Chung-Ang University, South Korea). We also thank Prof. Yong-Seok Lee (Seoul National University,
797 Seoul, South Korea) and Prof. Sung Hyun Kim (Kyung Hee University, Seoul, South Korea) for their
798 scientific comments on the synaptic functions of neurons.

799 **AUTHOR CONTRIBUTIONS**

800 Overall scientific conceptualization, J-WK; Methodology and investigation, M-JA, J-YK, JP, JhK, D-HK,
801 G-SS, H-ML, C-HK, MJK, and J-WK; Data analysis & scientific comments, M-JA, J-YK, JP, JhK, D-HK,
802 JkK, SR, S-BS, and J-WK; Statistical & bioinformatics analysis, JP, JhK; Writing original draft, M-JA, J-
803 YK, and J-WK; Funding acquisition, J-WK; Supervision and project administration, J-WK.

Figure 1

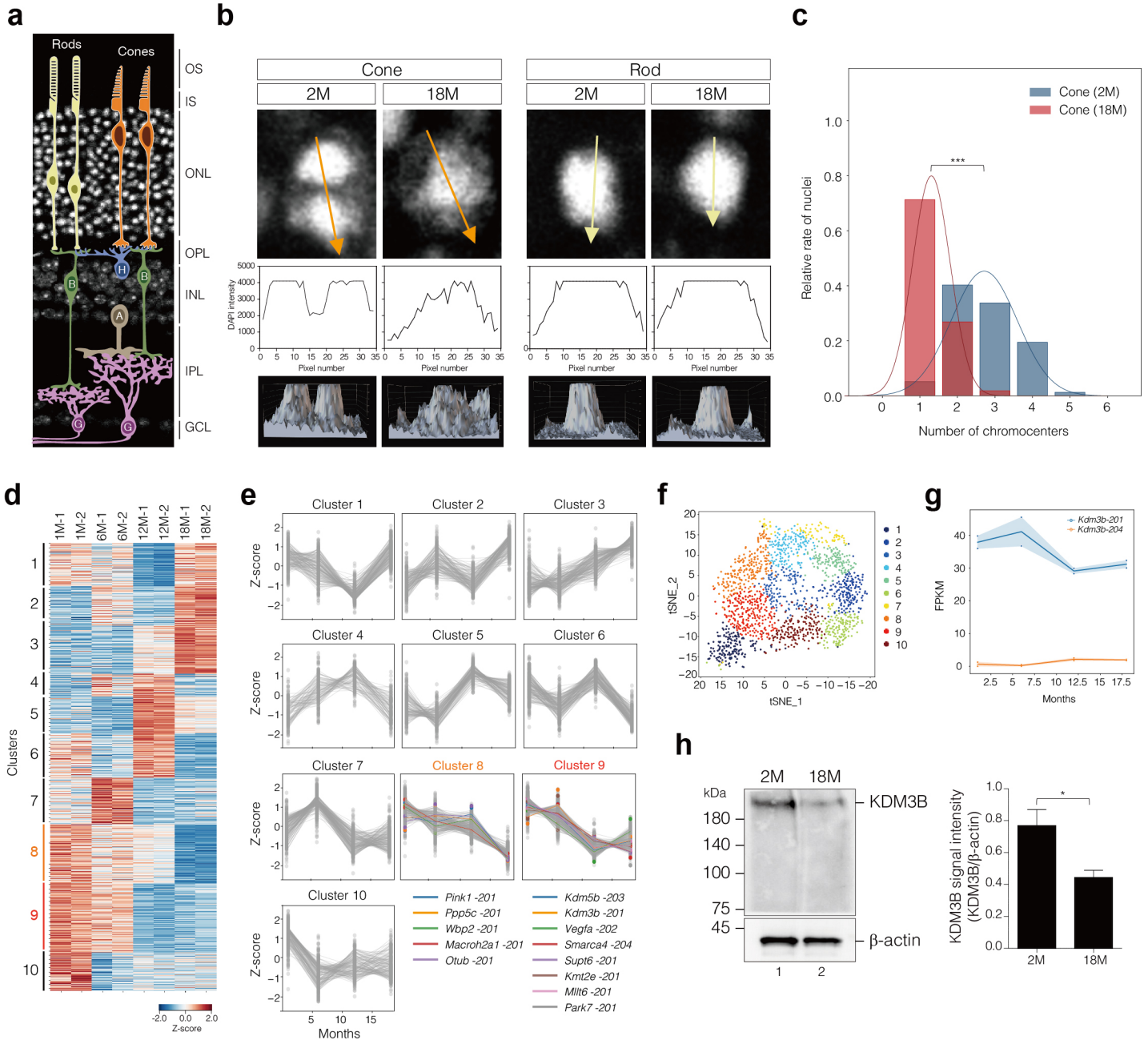


Fig. 1 Characterization of heterochromatin organization and transcriptomic profiling involved during retinal aging. **a**, Schematic representation of retinal structure. A; amacrine, B; bipolar. G; ganglion. H; horizontal cells. **b**, Representative immunofluorescence confocal images of mouse retinas stained using 4',6-diamidino-2-phenylindole (DAPI). **c**, Quantification of the number of chromocenters in nuclei of cones. **d**, Hierarchically clustered heatmap of transcripts (a total of 1,615 annotated transcripts (pre-filtered by FPKM > 30) that were differentially expressed in 1-, 6-, 12-, and 18-month-old C57BL/6J mouse retinas). **e**, Cluster analysis was performed by the K-means method for the gene expression profiles. **f**, tSNE plot revealing 10 distinct clusters identified from 1-, 6-, 12-, and 18-month-old C57BL/6J mouse retinas. **g**, The expression level of Kdm3b transcripts in 1-, 6-, 12-, and 18-month-old C57BL/6J mouse retinas. **h**, Whole retinal lysates of 2- and 18-month-old C57BL/6J mouse were immunoblotted using anti-KDM3B antibody. β -actin was used for internal loading control. Signal intensity of KDM3B was quantified using ImageJ software.

Figure 2

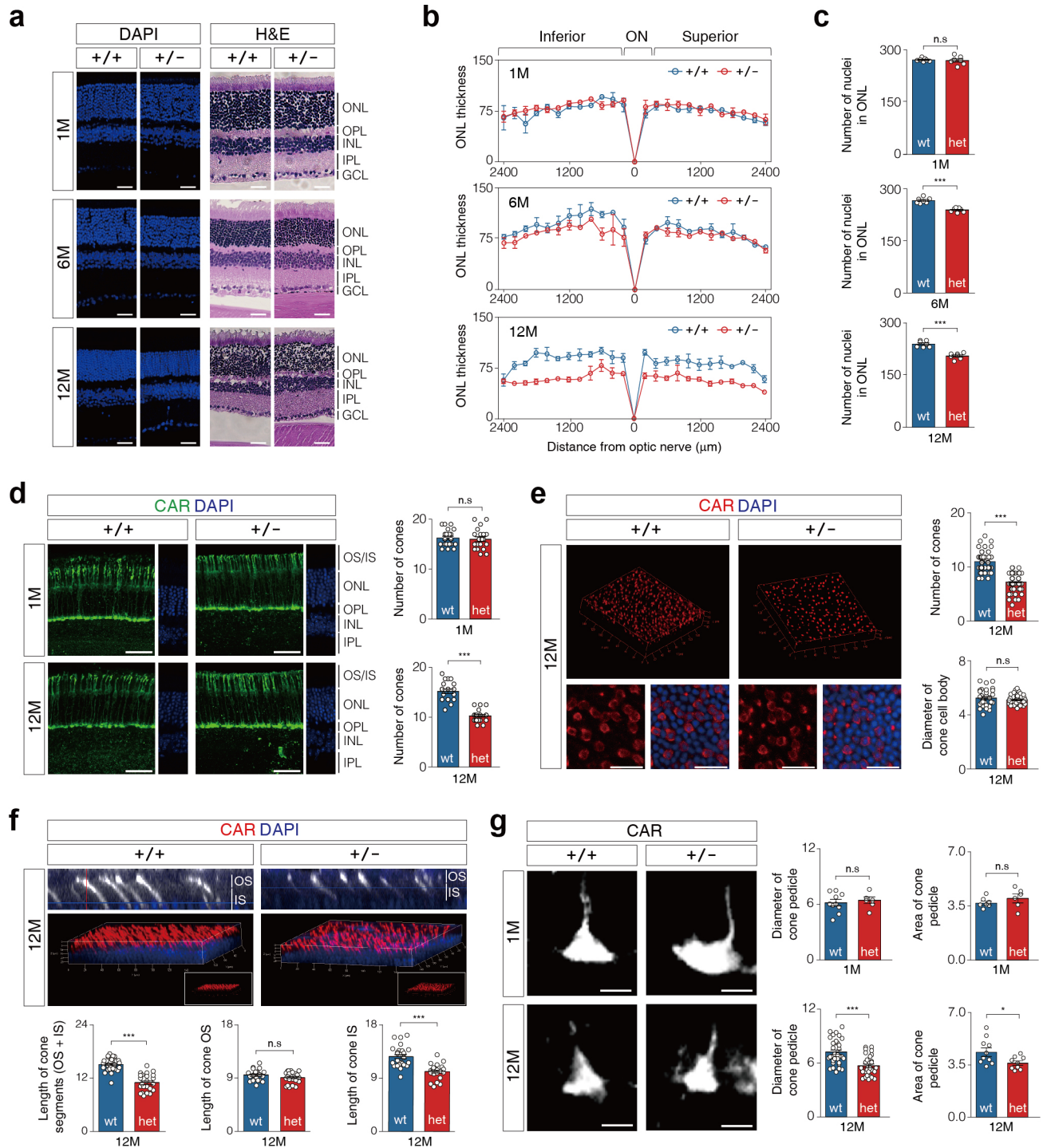


Fig. 2 The morphological changes in rods and cones in $Kdm3b^{+/-}$ mouse retinas. **a**, Cross-sectioned retinas are stained with DAPI and H&E from 1-, 6-, and 12-month-old $Kdm3b^{+/+}$ and $Kdm3b^{+/-}$ mice. Scale bar: 20 μm . **b**, Measurements of ONL thickness were made along the vertical axes of the eyes in 1, 6, and 12-month-old $Kdm3b^{+/+}$ and $Kdm3b^{+/-}$ mice ($n \geq 6$). **c**, Quantification of the number of nuclei in ONL in 100 μm^2 of retina. **d**, Immunostaining of cone arrestin (CAR) in 1- and 12-month-old $Kdm3b^{+/+}$ and $Kdm3b^{+/-}$ mouse retinas (left). Scale bar, 40 μm . The number of cones in 100 μm^2 of retina is quantified (right). **e, f**, Whole-mount retinas stained with CAR antibodies (red) in 12-month-old $Kdm3b^{+/+}$ and $Kdm3b^{+/-}$ mice. The number of cones and diameter of the cone cell body (μm) (**e**), and the length of cone segments (μm) (**f**) were measured. **g**, Cone pedicles in 12-month-old $Kdm3b^{+/+}$ and $Kdm3b^{+/-}$ mouse retinas (left). Scale bar: 10 μm . The diameter of cone pedicles (μm) and area of cone pedicles ($\text{pixel} \times 10^3$) were measured (right). Error bars show mean \pm SEM. P values obtained by Student's t-test. *** $P < 0.001$, * $P < 0.05$, n.s., not significant. OS; outer segment, IS; inner segment, ONL; outer nuclear layer, OPL; outer plexiform layer, INL; inner nuclear layer, IPL; inner plexiform layer, GCL; ganglion cell layer.

Figure 3

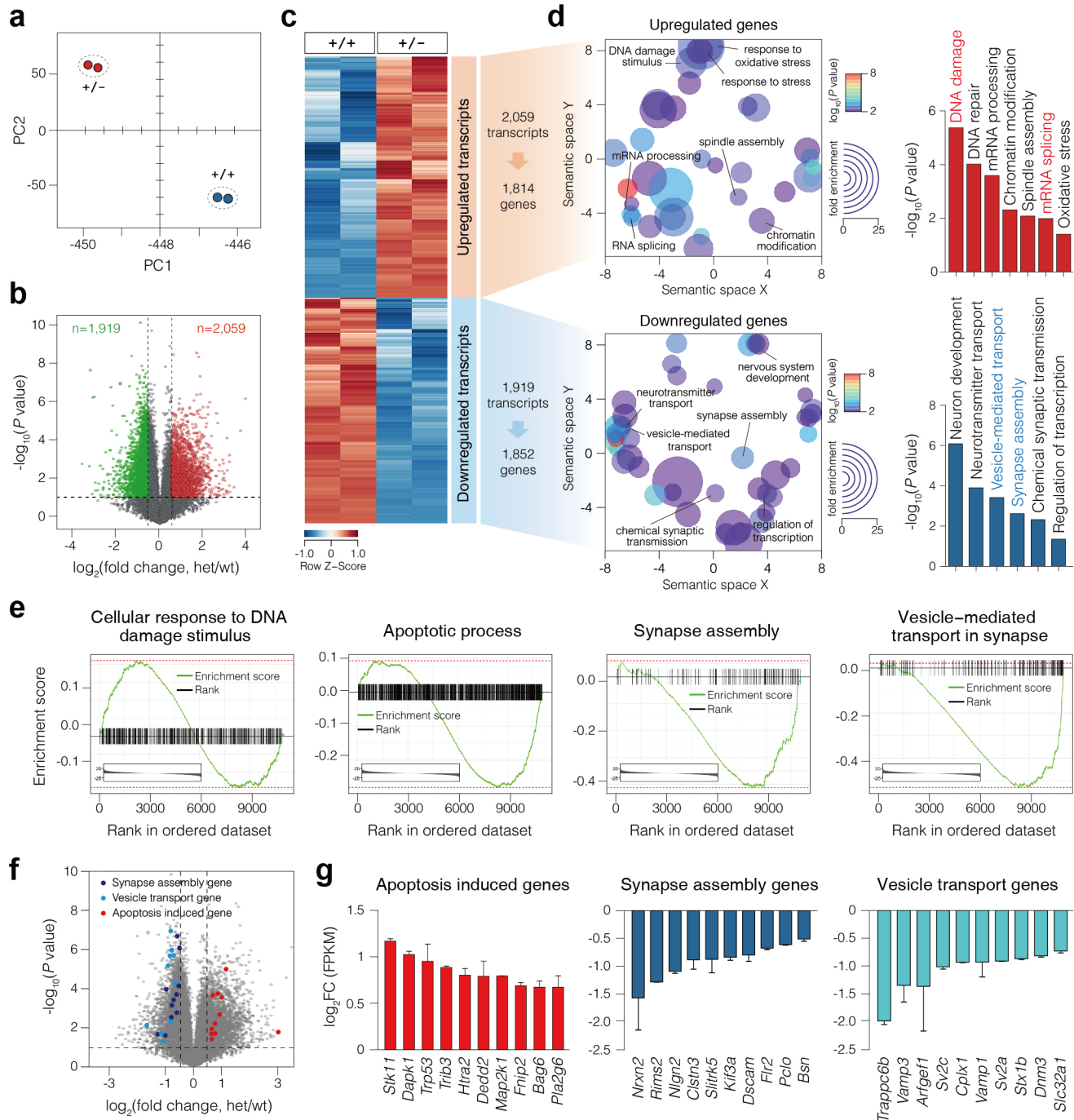


Fig. 3 Alteration of transcriptomic dynamics in *Kdm3b*^{+/-} mouse retinas. **a**, PCA plot of RNA-sequencing from 12-month-old *Kdm3b*^{+/+} and *Kdm3b*^{+/-} mouse retinas. Small circles symbolize each sample, and larger circles indicate each group. **b**, Volcano plot showing changes of gene expression patterns in *Kdm3b*^{+/+} and *Kdm3b*^{+/-} mice. Expressed transcripts with strict filtering ($\log_2\text{FC} > 0.5$, $P \text{ value} < 0.05$) highlight only upregulated (red dots) and downregulated (green dots) transcripts. **c**, Hierarchical clustering of transcripts from volcano plot (a total of 3,978 transcripts) in *Kdm3b*^{+/+} and *Kdm3b*^{+/-} mice. A clear alteration in transcriptome landscape is obvious between *Kdm3b*^{+/+} and *Kdm3b*^{+/-} mouse retinas. **d**, Scatter plot of confidence scores for enriched gene ontologies associated with differentially expressed genes, with ontologies clustered by functional similarity in the semantic space (left). Gene ontology of biological process is identified by the DAVID showing upregulated and downregulated genes in *Kdm3b*^{+/-} mouse retinas (right). **e**, GSEA scores for genes involved in cellular responses to DNA damage stimuli, apoptotic processes, synapse-assembly, and vesicle-mediated transport in synapses. **f**, Volcano plot described in (b) with three gene set categories: apoptosis-induced genes (red), synapse assembly genes (blue), and vesicle-mediated transport genes (cyan). **g**, Expression of genes in three categorized groups is represented in \log_2 of fold-change (FPKM). When multiple transcripts are expressed, the expression level of the most highly expressed transcript is indicated. Error bars show mean \pm SEM.

Figure 4

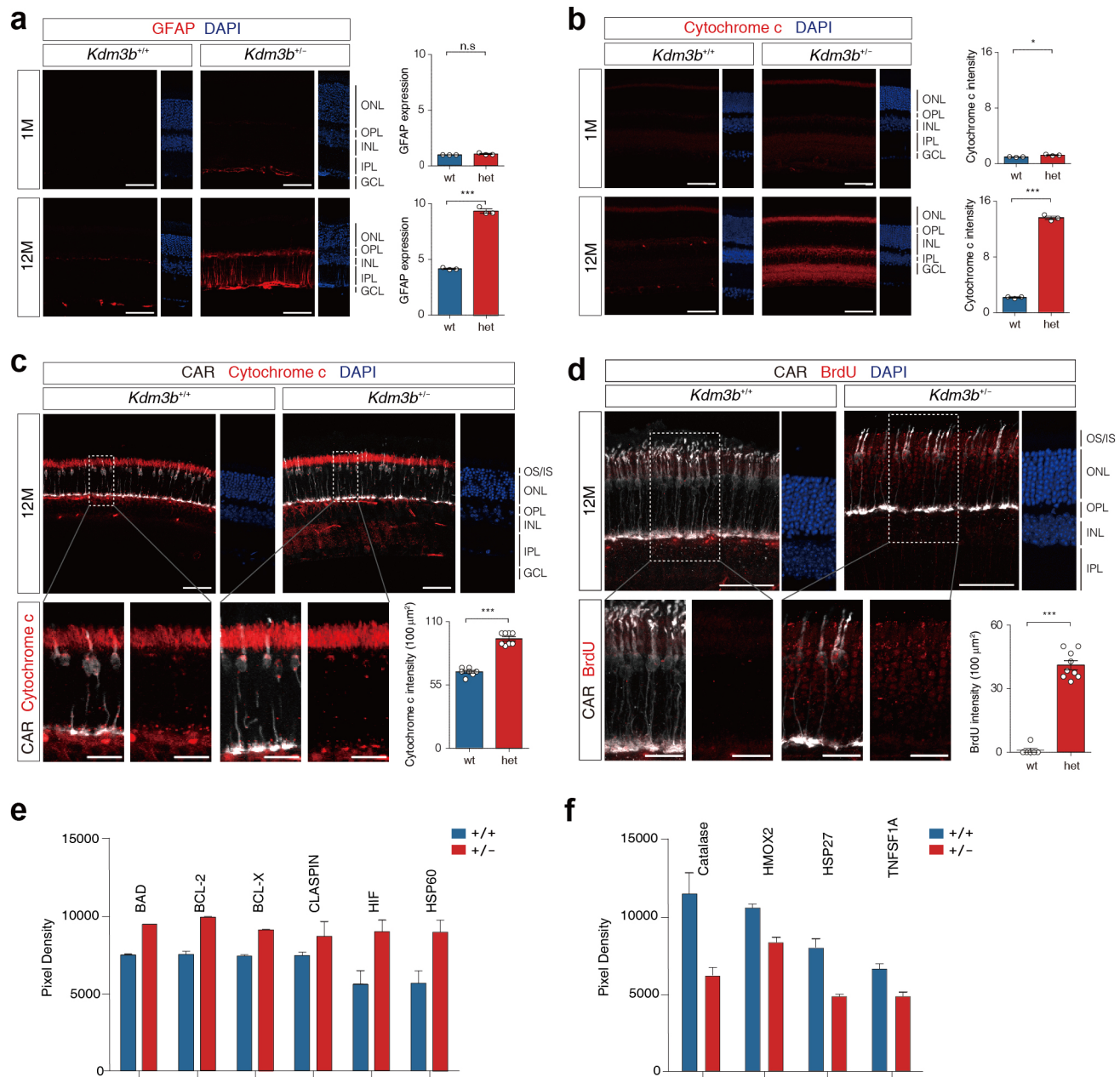


Fig. 4 Induction of apoptotic response of cones in *Kdm3b*^{+/-} mice. **a**, Immunostaining of glial fibrillary acidic protein (GFAP) for the specific staining of Müller glial cells in 1- and 12-month-old *Kdm3b*^{+/+} and *Kdm3b*^{+/-} mice (left). Scale bar: 40 μ m. GFAP-intensity of Müller glial cells was measured using ImageJ software in 1- and 12-month-old *Kdm3b*^{+/+} and *Kdm3b*^{+/-} retinas (right). **b**, Immunostaining of cytochrome c in 1- and 12-month-old *Kdm3b*^{+/+} and *Kdm3b*^{+/-} retinas (left). Scale bar: 40 μ m. Cytochrome c intensity of the retinas in 1- and 12-month-old *Kdm3b*^{+/+} and *Kdm3b*^{+/-} mice was measured using ImageJ (right). **c**, Double immunostaining of cytochrome c (red) and CAR (white) in 12-month-old *Kdm3b*^{+/+} and *Kdm3b*^{+/-} retinas. Scale bar: 40 μ m. High magnification images in the white box showing cytochrome c (red) expression in cones (white arrowhead). Scale bar: 20 μ m. The signal intensity of cytochrome c-positive cones was measured. **d**, Apoptotic cells were detected by TUNEL assay (BrdU positive cells) in 12-month-old *Kdm3b*^{+/+} and *Kdm3b*^{+/-} retinas. Scale bar: 50 μ m. High magnification images in the white box showing BrdU (red) staining in cone photoreceptors (white). Scale bar: 20 μ m. The percentage of BrdU-positive cones. Error bars show mean \pm SEM. *P* values obtained by Student's *t*-test. *** *P* < 0.001, * *P* < 0.05, n.s, not significant. **e, f**, Relative protein expression levels were estimated after quantifying the pixel densities in autoradiograms using ImageJ.

Figure 5

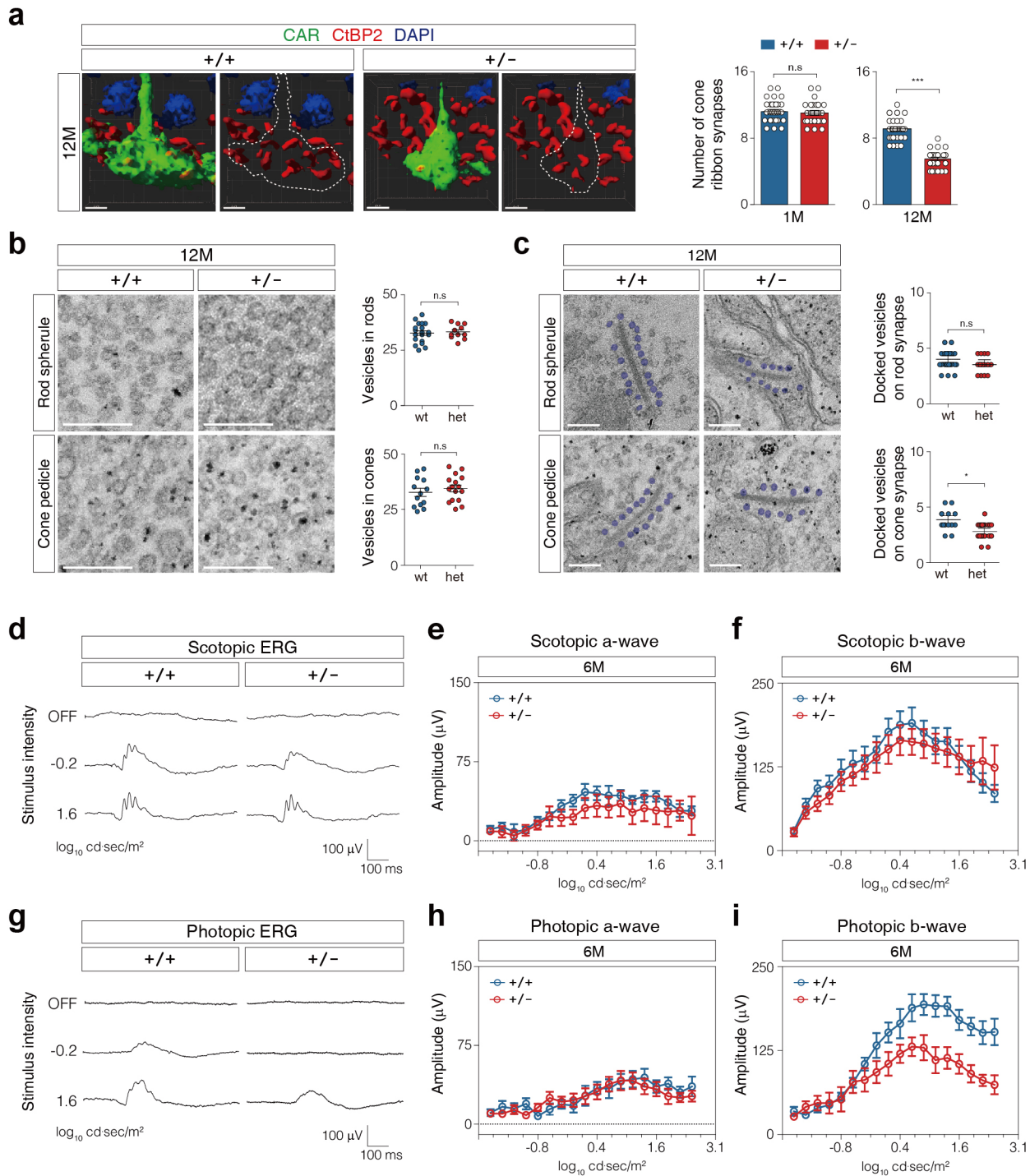


Fig. 5 The alteration of synaptic morphology of cones in *Kdm3b*^{-/-} mice. **a**, 3D reconstruction images showing ribbon synapses in the cone photoreceptors of 12-month-old *Kdm3b*^{+/+} and *Kdm3b*^{+/-} mice. Scale bar: 5 μ m. Immunostaining with CtBP2 (C-terminal binding protein) and CAR antibodies examined in 1 and 12-month-old *Kdm3b*^{+/+} and *Kdm3b*^{+/-} mice (left). The number of ribbon synapses is measured in a single cone pedicle (right). Scale bar: 2 μ m. **b**, Transmission electron microscopy (TEM) images of the vesicles in rod spherules and cone pedicles of 12-month-old *Kdm3b*^{+/+} and *Kdm3b*^{+/-} mice (left). The number of vesicles in a single rod spherule and cone pedicle (0.16 μ m²) (right). Scale bar: 0.2 μ m. **c**, TEM images of docked vesicles (shaded with light cyan) near the rod and cone ribbon synapse (left). Scale bar: 0.2 μ m. The number of docked vesicles near the rod and cone ribbon synapse in 12-month-old *Kdm3b*^{+/+} and *Kdm3b*^{+/-} mice (0.1 μ m of each ribbon synapse) (right). Error bars show mean \pm SEM. *P* values obtained by Student's *t*-test. * *P* < 0.05, n.s., not significant. **d-i**, Electroretinograms (ERGs) of 6-month-old *Kdm3b*^{+/+} and *Kdm3b*^{+/-} mice in 17 different stimulus flashes (from -1.7 to 3.1 \log_{10} cd μ sec/m²) presented in darkness (scotopic) and superimposed upon a steady rod-desensitizing adapting field (photopic). **d**, Representative scotopic ERGs elicited by two different stimuli (OFF, -0.1, and 1.6 \log_{10} cd μ sec/m²) from 6-month-old *Kdm3b*^{+/+} and *Kdm3b*^{+/-} mice. **e**, **f**, The scotopic amplitudes of a-waves (**e**) and b-waves (**f**) are shown as functions of the stimulus intensity. **g**, Representative photopic ERGs elicited by two different stimuli (OFF, -0.1, and 1.6 \log_{10} cd μ sec/m²) from 6-month-old *Kdm3b*^{+/+} and *Kdm3b*^{+/-} mice. **h**, **i**, The photopic amplitudes of a-waves (**h**) and b-waves (**i**) are shown as functions of the stimulus intensity. Graphs show the mean \pm SEM, *n* = 7 per each genotype.

Figure 6

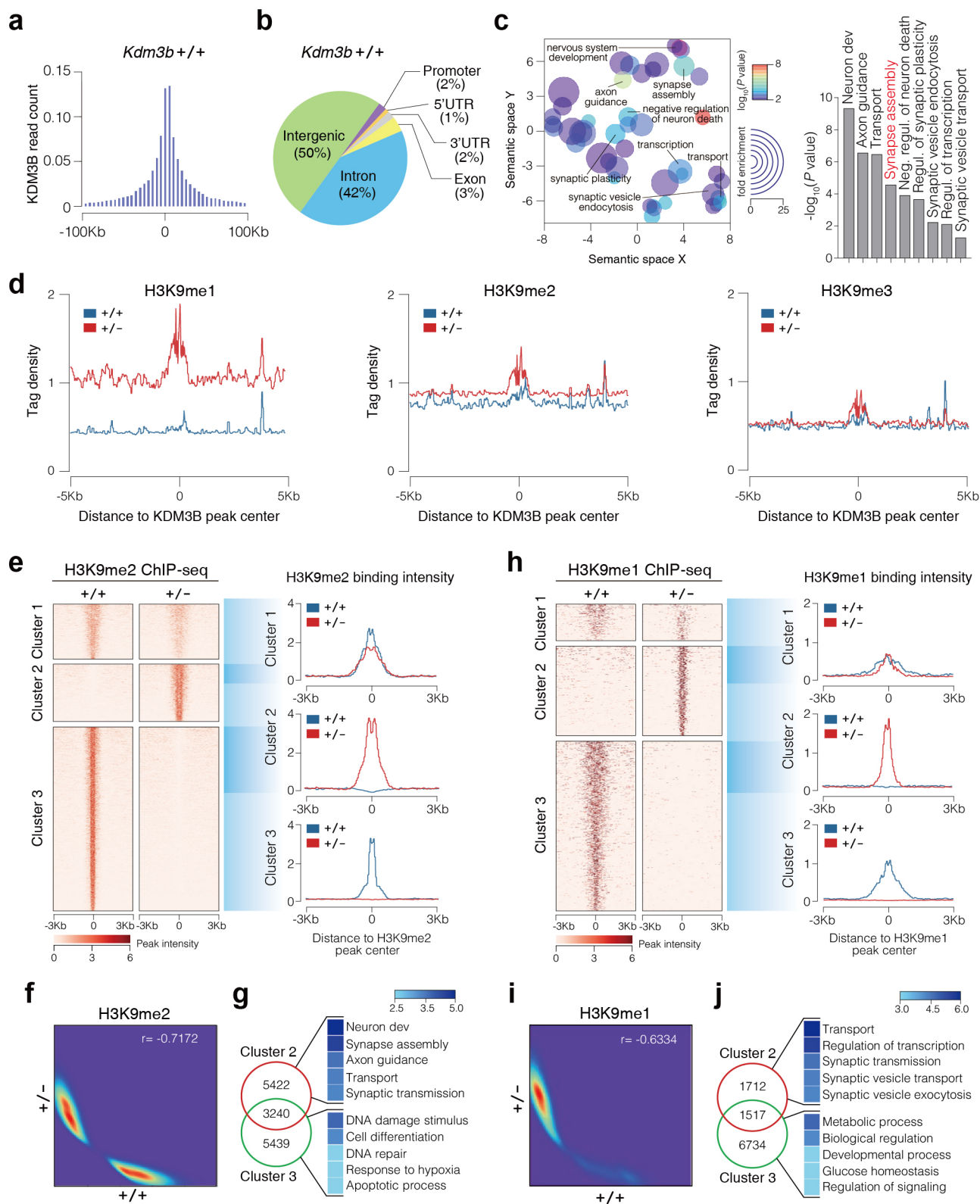


Fig. 6 The disruption of global H3K9 methylation in *Kdm3b*^{+/-} mouse retinas. **a**, Bar graph shows the distribution of KDM3B peaks around transcriptional start sites. **b**, Pie chart of KDM3B enrichment distribution at genomic loci within the genome, including promoters, exons, introns, 5'-untranslated regions (5'-UTRs), 3'-UTRs, and intergenic regions (outside -10 to +10 Kb of genes) in *Kdm3b*^{+/+} mouse retinas. **c**, Scatter plot of confidence scores for enriched gene ontologies associated with KDM3B ChIP-seq signal, with ontologies clustered by functional similarity in the semantic space (left). Gene ontology of biological process is identified by the DAVID showing KDM3B-enriched peaks (right). **d**, Plots of H3K9me1, H3K9me2, and H3K9me3 ChIP-seq signal intensity relative to the center of KDM3B occupied sites (± 5 Kb) in *Kdm3b*^{+/+} and *Kdm3b*^{+/-} mouse retinas. **e**, **h**, Heatmap view of H3K9me2 (**e**) and H3K9me1 (**h**) ChIP-Seq-read intensity around H3K9me2 (**e**) and H3K9me1 (**h**) peak center (± 3 Kb) detected in *Kdm3b*^{+/+} and *Kdm3b*^{+/-} mouse retinas. The plot shows the mean H3K9me2 and H3K9me1 binding intensities to the center of each peak. **f**, **i**, Scatter density plot of input-normalized H3K9me2 (**f**), and H3K9me1 (**i**) RPKM between *Kdm3b*^{+/+} and *Kdm3b*^{+/-} at H3K9me2 peak TSS regions (**f**), and at H3K9me1 peak TSS regions (**i**). **g**, **j**, Gene ontology of biological process is identified by the DAVID showing H3K9me2 (**g**) and H3K9me1 (**j**) enriched peaks in *Kdm3b*^{+/+} and *Kdm3b*^{+/-} mouse retinas.

Figure 7

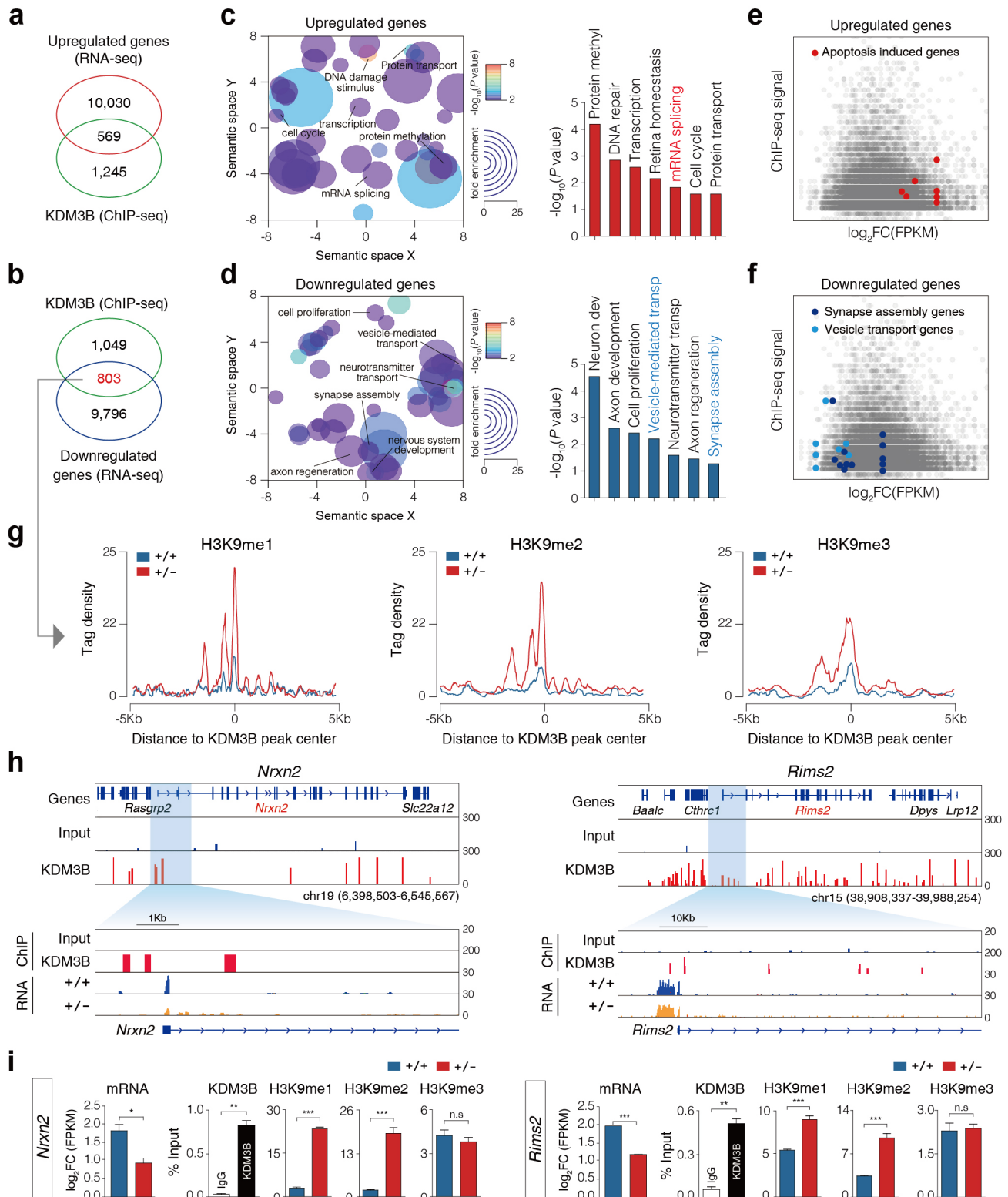


Fig. 7 The global correlation between transcriptome and epigenome dynamics during mouse retinal aging. **a, b**, Venn diagram showing the overlap between the genes including KDM3B peaks and upregulated (**a**) or downregulated (**b**) KDM3B-target genes based on RNA-sequencing data. **c, d**, Scatter plot of confidence scores for enriched gene ontologies associated with upregulated genes (**c**) and downregulated genes (**d**) and their enrichments for KDM3B, with ontologies clustered by functional similarity in the semantic space. Gene ontology of biological process shows upregulated and downregulated genes integrated with RNA-sequencing and ChIP-seq analysis. **e, f**, Scatter plot showing changes in expression of upregulated (**e**) or downregulated genes (**f**) in *Kdm3b*^{+/+} and *Kdm3b*^{+/-} mouse retinas and their enrichments for KDM3B. **g**, Plots of H3K9me1, H3K9me2, and H3K9me3 ChIP-seq signal intensity relative to the center of downregulated KDM3B occupied sites ($\pm 5\text{Kb}$) in *Kdm3b*^{+/+} and *Kdm3b*^{+/-} mouse retinas. **h**, ChIP-seq tracks of KDM3B in *Kdm3b*^{+/+} along the *Nrxn2* and *Rims2* locus. Selected genomic elements (shaded with light cyan) indicate KDM3B ChIP-seq peaks at *Nrxn2* and *Rims2* promoter regions. **i**, Recruitment and presence of KDM3B, H3K9me1, H3K9me2, and H3K9me3 at *Nrxn2* and *Rims2* promoter regions are validated by ChIP-qPCR. Results are presented as the mean \pm SEM (error bars). *P* values obtained by Student's t-test. *** *P* < 0.001, ** *P* < 0.01, n.s, not significant.

Figure 8

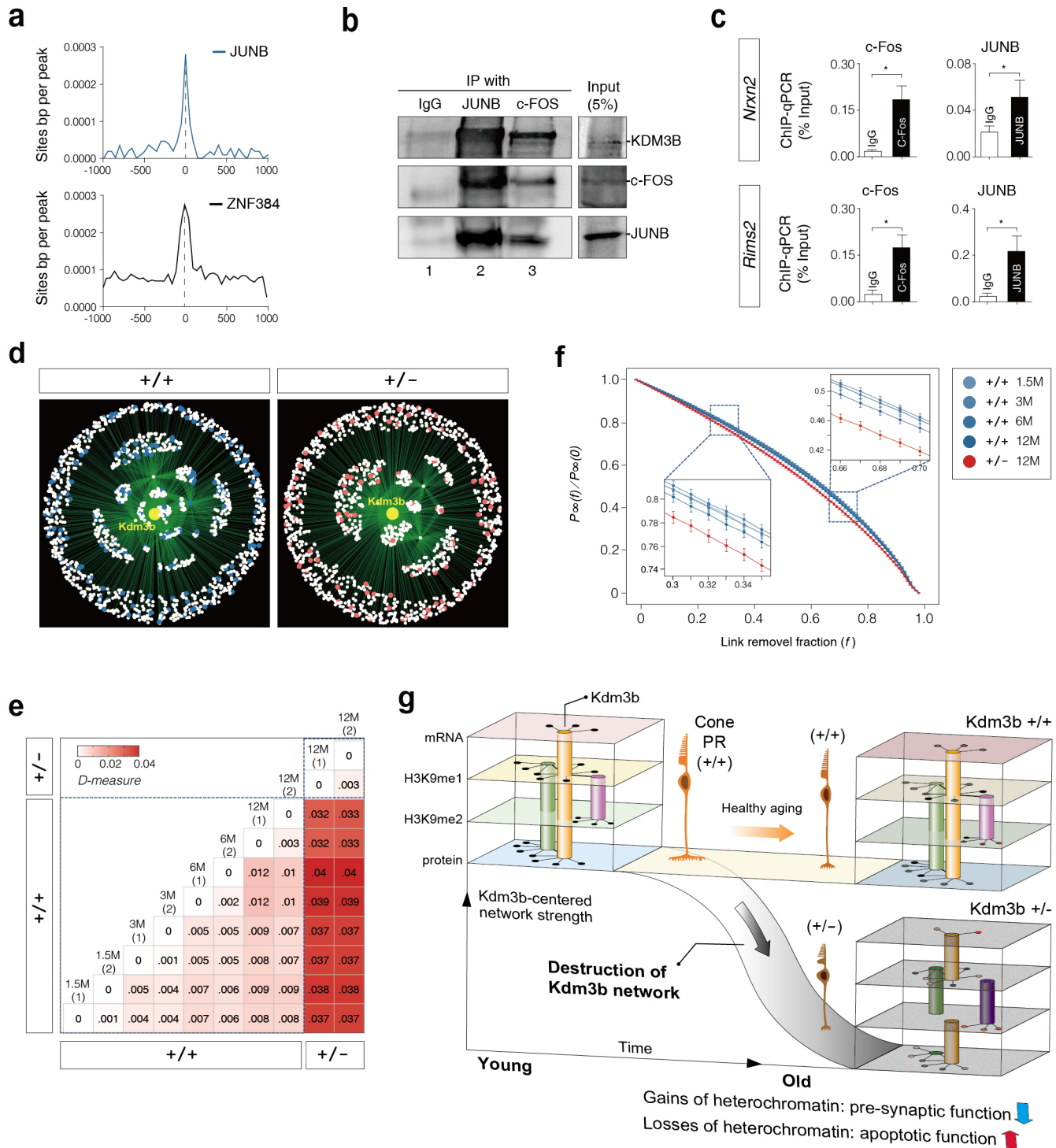
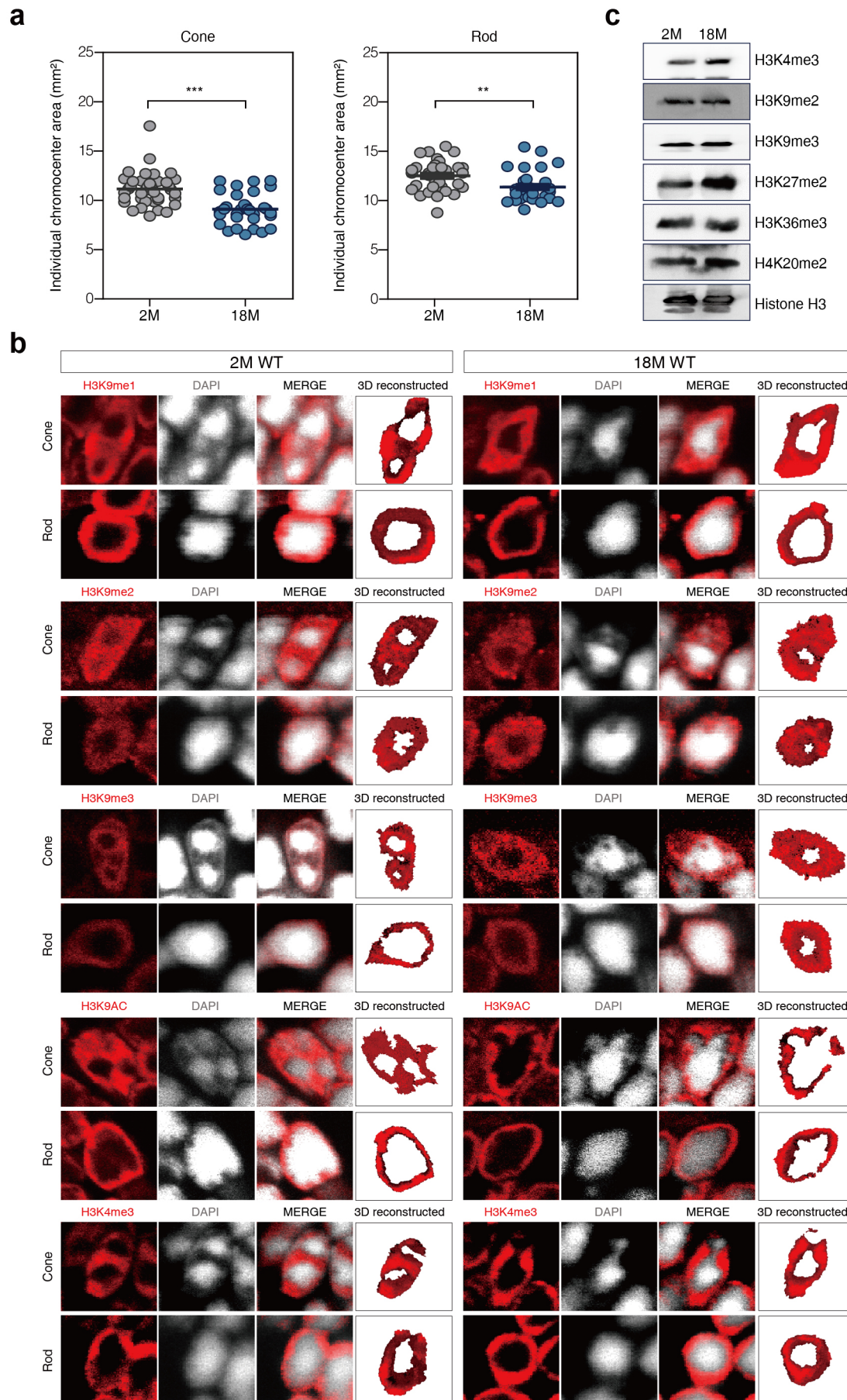


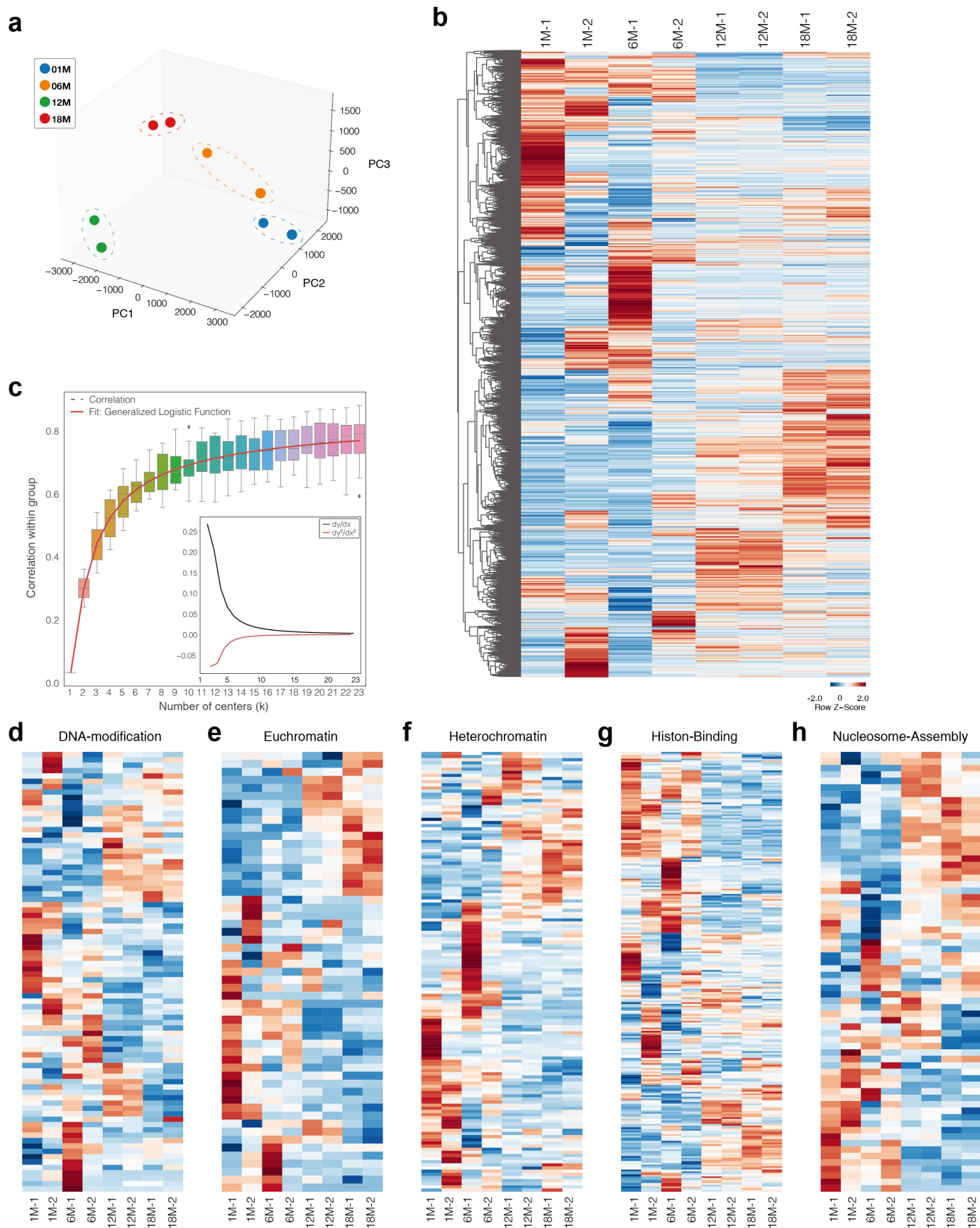
Fig. 8 The measurement of structural difference and robustness of KDM3B-centered networks. **a**, The graph represents the distribution of occurrence probabilities of the consensus sequences enriched under KDM3B ChIP-Seq peaks with respect to ZNF384 and JUN motifs. **b**, Immunoblot showing co-immunoprecipitation of endogenous KDM3B with c-Fos and JUNB in mice retinas. **c**, Recruitment and presence of c-Fos and JUNB at *Nrxn2* and *Rims2* promoter regions are validated by ChIP-qPCR. Error bars show mean \pm SEM. P values obtained by Student's t-test. * $P < 0.05$. **d**, The KDM3B-centered networks in *Kdm3b*^{+/+} and *Kdm3b*^{+/-} mouse retinas. The circles indicate individual nodes (i.e., regulator and target genes), and the line indicates the interaction between regulatory hubs and genes. The KDM3B-centered network is shown as a yellow circle in the center of networks. The differential expression nodes are represented by the blue circles (downregulated genes in *Kdm3b*^{+/-}) and red circles (upregulated genes in *Kdm3b*^{+/-}). **e**, The matrix of dissimilarity D's measured from each pair of networks. **f**, The plot of fraction of nodes that belong to the largest component in the network for link removal fraction f . All quantities are averaged over 300 realizations for each network. The error bars are estimated from all realizations. **g**, Schematic representation of KDM3B-centered network during mouse retinal aging. The integrated KDM3B-centered network with gene expression (mRNA), chromatin status (H3K9me1, H3K9me2), protein was visualized in the cube. Subtle change of network strength in *Kdm3b*^{+/-} mouse retina leads to the breakdown of functional physiology in the cone photoreceptors.

Extended Data Fig. 1



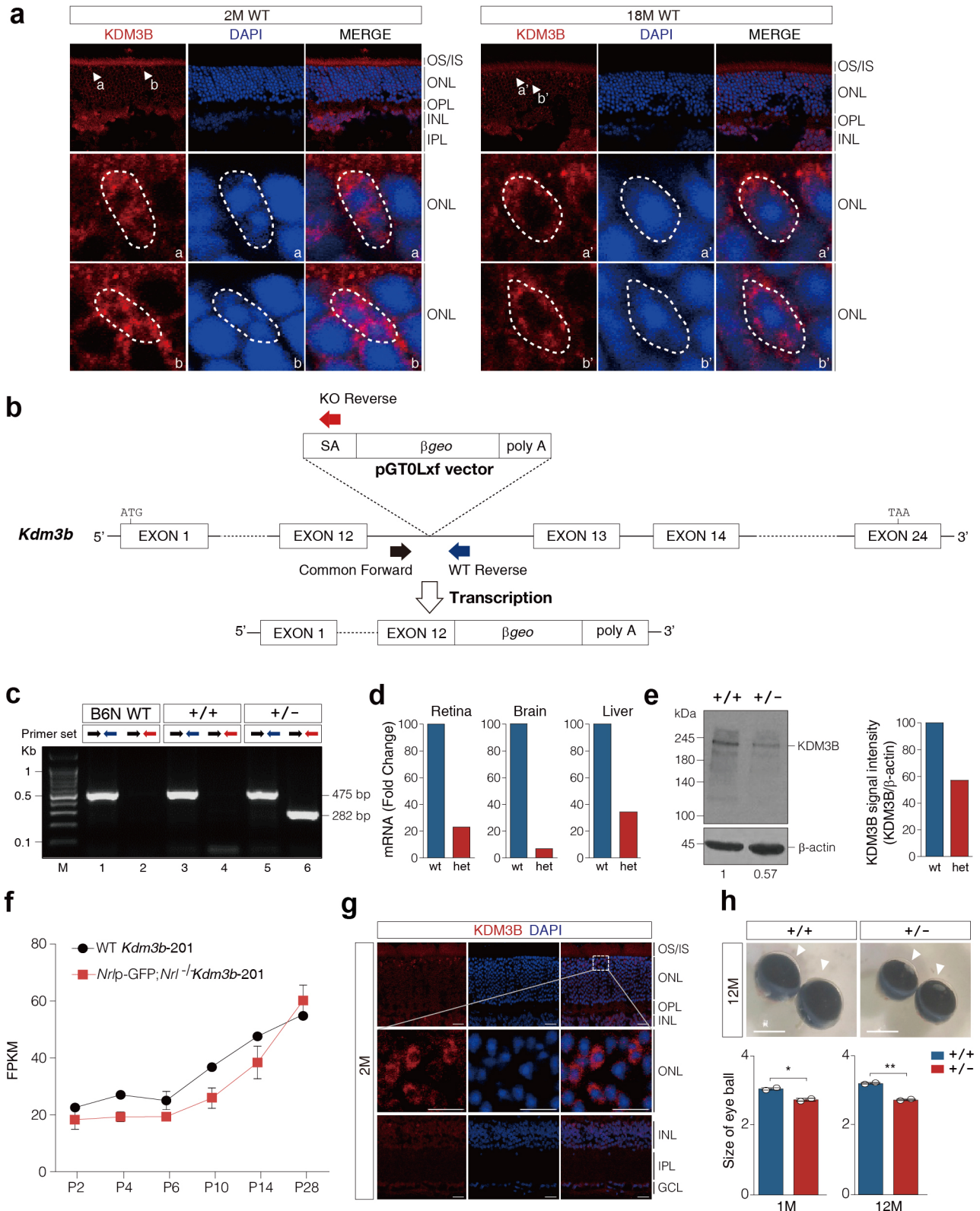
Extended Data Fig. 1 Characterization of heterochromatin organization during retinal aging. **a**, The area of chromocenter (μm^2) in cone and rod. **b**, Whole retinal lysates of 2- and 18-month-old *Kdm3b*^{+/+} mice were immunoblotted using histone specific modification antibodies. Histone H3 antibody was used for internal loading control. **c**, Immunostaining of histone mark (red) and DAPI in 2- and 18-month-old *Kdm3b*^{+/+} mouse retinas.

Extended Data Fig. 2



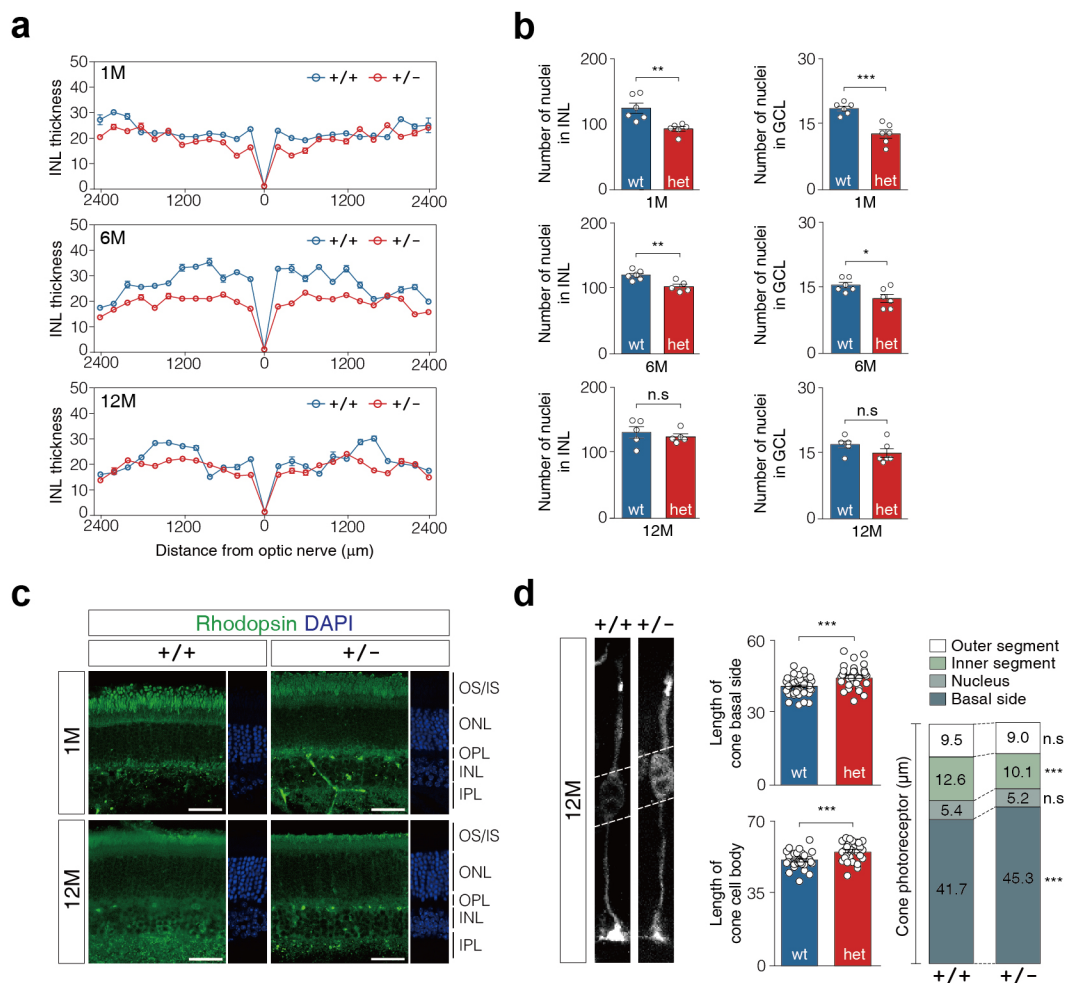
Extended Data Fig. 2 Transcriptomic profiling during retinal aging. **a**, PCA plot of RNA-seq from 1-, 6-, 12- and 18-months mouse retinas. **b**, Hierarchically clustered heatmap of transcripts (a total of 19,484 annotated transcripts were prefiltered by FPKM > 1 that were differentially expressed in 1-, 6-, 12- and 18-months mouse retinas). **c**, Plot of correlation within group for the number of k centers and fitting the data with generalized logistic function. Inset of **(c)**: Plots of first and second-order to the fitted function. **d-h**, Hierarchically clustered heatmap of transcripts involved in DNA-modification, euchromatin, heterochromatin, histone-binding, and nucleosome-assembly.

Extended Data Fig. 3



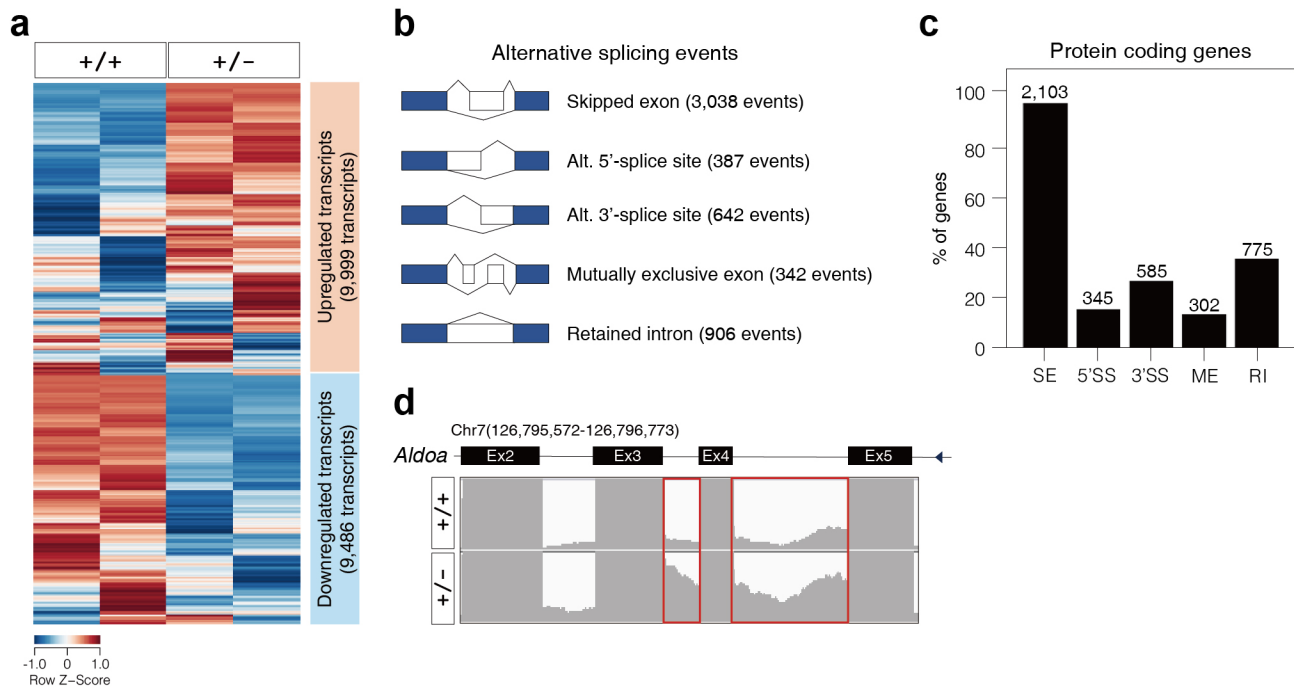
Extended Data Fig. 3 Generation of *Kdm3b*^{+/-} mice. **a**, Immunostaining of KDM3B (red) and DAPI in 2- and 18-month-old *Kdm3b*^{+/+} mouse retinas. **b**, Gene trap vector (pGT0Lxf) was inserted into the intron region between exon 12 and exon 13. **c**, Genotyping of *Kdm3b*^{+/+} and *Kdm3b*^{+/-} mice was performed by conventional PCR analysis using isolated genomic DNA (gDNA) from mouse tails representing each genotype. The bands of 475 bp and 282 bp correspond to WT and mutant alleles, respectively. **d**, qRT-PCR analysis of *Kdm3b* mRNA expression (fold-change) in retina, brain, and liver of *Kdm3b*^{+/+} and *Kdm3b*^{+/-} mice. **e**, Whole retinal lysates of *Kdm3b*^{+/+} and *Kdm3b*^{+/-} mice were immunoblotted using anti-KDM3B antibody (left). β-actin was used for internal loading control. Signal intensity of KDM3B was quantified using ImageJ software (right). **f**, Expression level of *Kdm3b* transcripts in whole retina (WT) and s-cone-like cells (*Nrlp-GFP;Nrl*⁻¹) plotted for six developmental time points (P2, P4, P6, P10, P14, and P28) using public RNA-sequencing data (GSE 74660). **g**, Immunostaining of KDM3B (red) and DAPI in 2-month-old *Kdm3b*^{+/+} mouse retinas. Scale bar: 20 μm. High magnification image in the white box showing KDM3B (red) staining in cones (middle panel). Scale bar: 10 μm. **h**, Eye balls were enucleated from 12-month-old *Kdm3b*^{+/+} and *Kdm3b*^{+/-} mice. White arrows indicate the abnormal cornea phenotype. Scale bar: 2 mm. The sizes of eye balls in 1- and 12-month-old *Kdm3b*^{+/+} and *Kdm3b*^{+/-} mice was measured. Error bars show mean ± SEM. *P* values obtained by Student's *t*-test. ** *P* < 0.01, * *P* < 0.05.

Extended Data Fig. 4



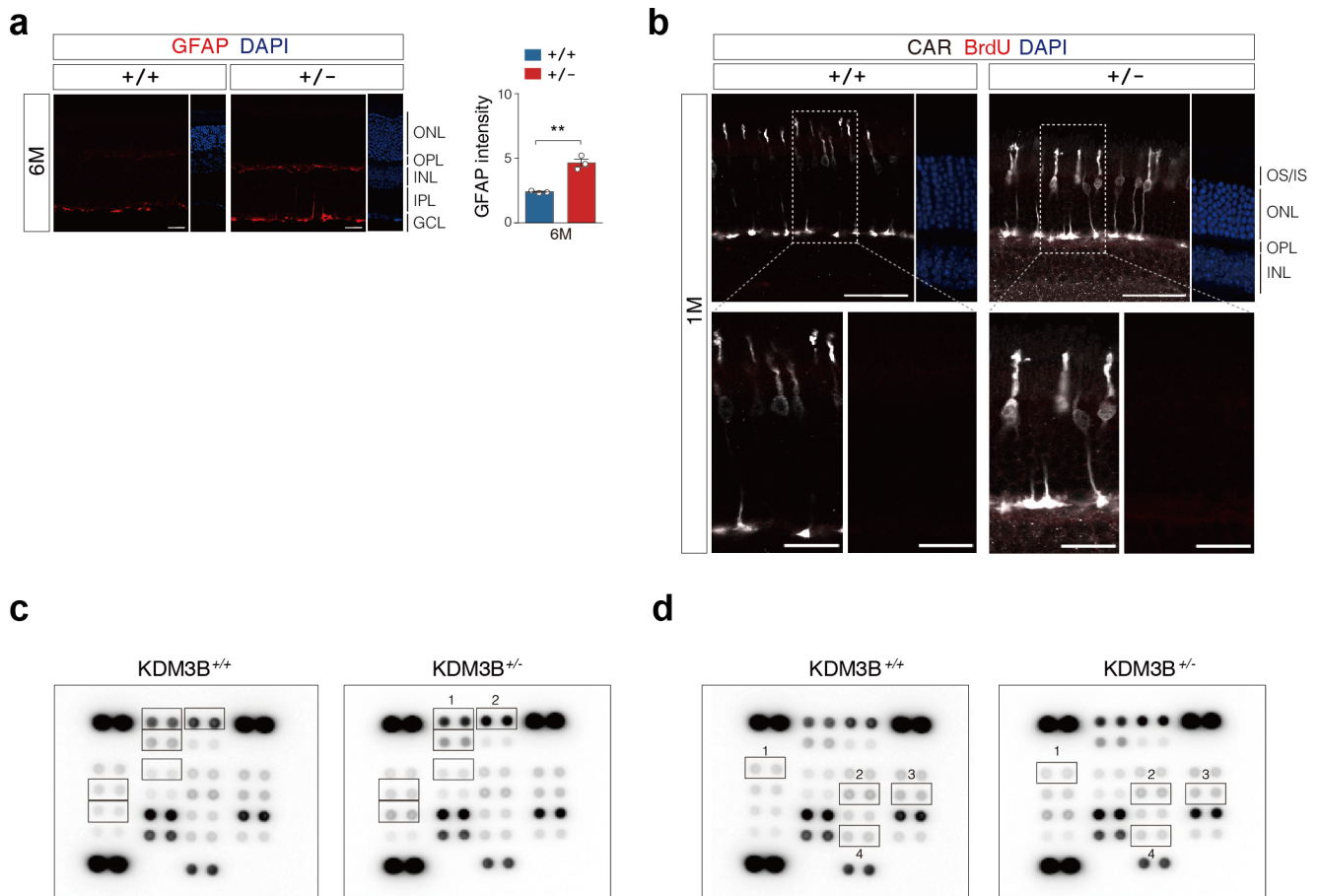
Extended Data Fig. 4 The morphological changes of rod and cone photoreceptors in *Kdm3b*^{+/-} mouse retinas. **a**, Thickness of INL was measured along the vertical meridians of the retinas of 1-, 6-, and 12-month-old *Kdm3b*^{+/+} and *Kdm3b*^{+/-} mice ($n \geq 6$). **b**, The number of nuclei in INL was quantified in 100 μm^2 of retina (left) and linearized GCL in 100 μm of retina (right). **c**, Immunostaining of rhodopsin (Rho) in 1 and 12-month-old *Kdm3b*^{+/+} and *Kdm3b*^{+/-} mouse retinas. Scale bar: 40 μm . **d**, Measurements of the length of cone basal side (μm) and cell body (μm) by ImageJ software. Error bars show mean \pm SEM. P values obtained by Student's t-test. *** $P < 0.001$, n.s., not significant.

Extended Data Fig. 5



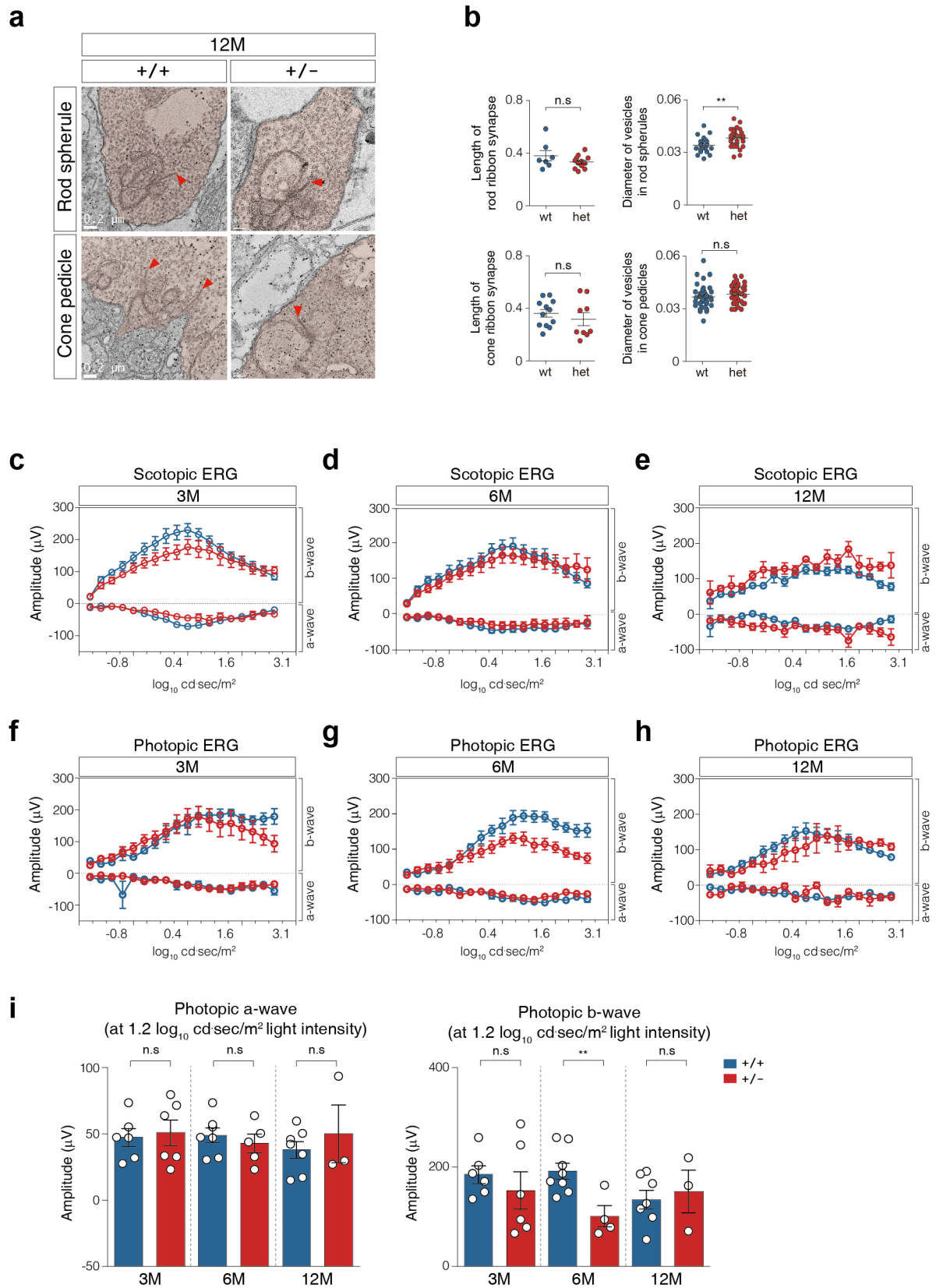
Extended Data Fig. 5 Alternative splicing in *Kdm3b*^{+/-} mouse retinas. **a**, Hierarchically clustered heatmap of transcripts (a total of 19,485 annotated transcripts (pre-filtered by FPKM > 1) that were differentially expressed in *Kdm3b*^{+/+} and *Kdm3b*^{+/-} mouse retinas). **b**, Alternative splicing events were analyzed with Rmats (v4.1), which identified 5,315 genes having alternative splicing events (P value < 0.05). Types of alternative splicing events detected and frequencies in group-wise comparisons. **c**, Protein coding genes obtained from alternative splicing events indicated as the percentages of counted genes. **d**, Differential retained introns between *Kdm3b*^{+/+} and *Kdm3b*^{+/-} mouse retinas. The genomic area of the *Aldoa* gene is shown, which comprises eight exons and seven introns, and RNA-sequencing coverage plots of *Kdm3b*^{+/+} and *Kdm3b*^{+/-} in the area of exons two through five. Red box indicates the clear retained intron region in *Kdm3b*^{+/-} mouse retinas.

Extended Data Fig. 6



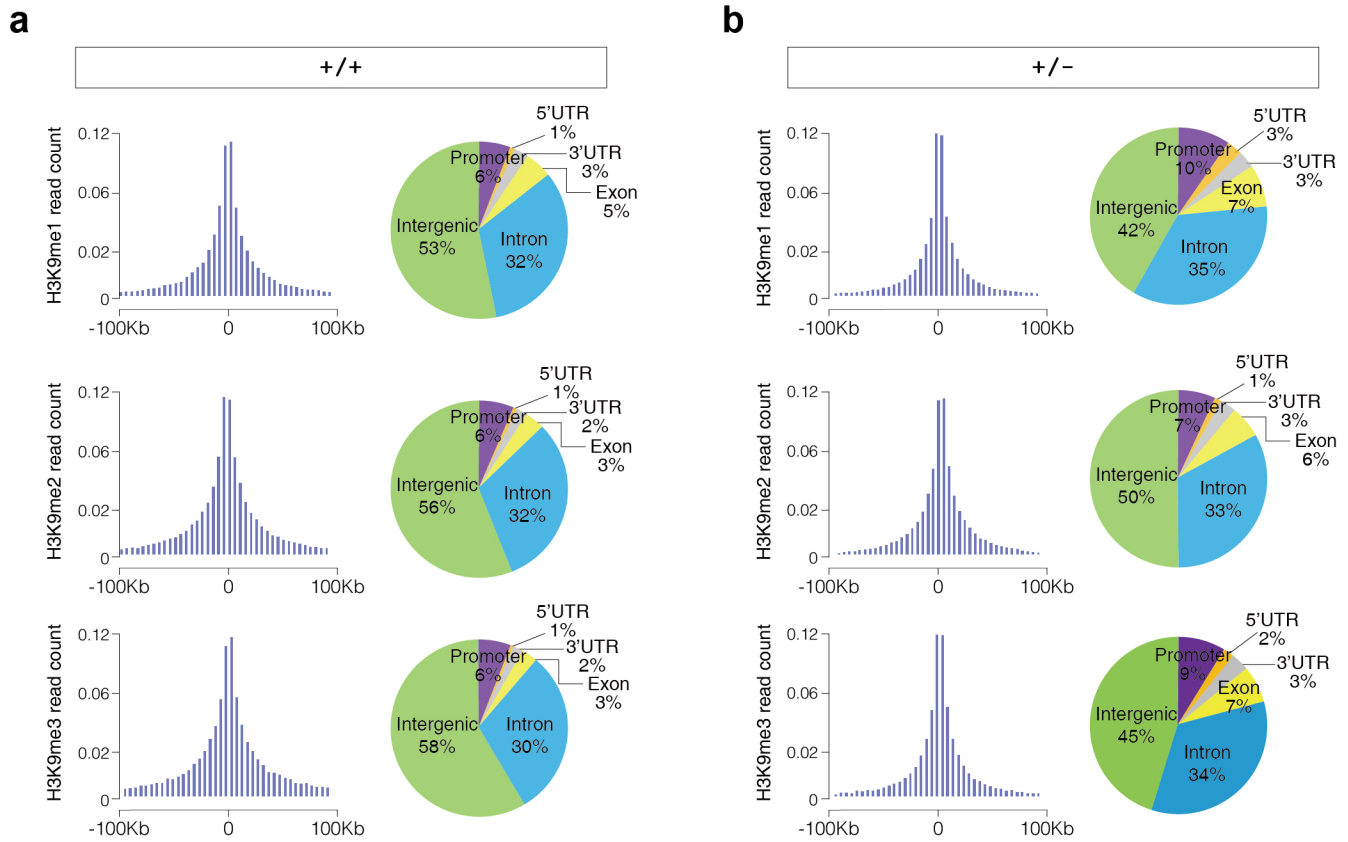
Extended Data Fig. 6 Increase of apoptotic cell death in cones in *Kdm3b*^{+/-} retinas. **a**, Immunostaining of GFAP in 6-month-old *Kdm3b*^{+/+} and *Kdm3b*^{+/-} mouse retinas (left). Scale bar: 20 μ m. GFAP-intensity of Müller glial cells was measured by ImageJ in 6-month-old *Kdm3b*^{+/+} and *Kdm3b*^{+/-} mouse retinas (right). **b**, Apoptotic cells were detected by TUNEL assay (BrdU positive cells) in 12-month-old *Kdm3b*^{+/+} and *Kdm3b*^{+/-} mouse retinas. Scale bar: 50 μ m. BrdU-positive cones in red dashed box. **c**, **d**, The entire apoptosis proteome profile array in 8-month-old *Kdm3b*^{+/+} and *Kdm3b*^{+/-} mouse retinas.

Extended Data Fig. 7



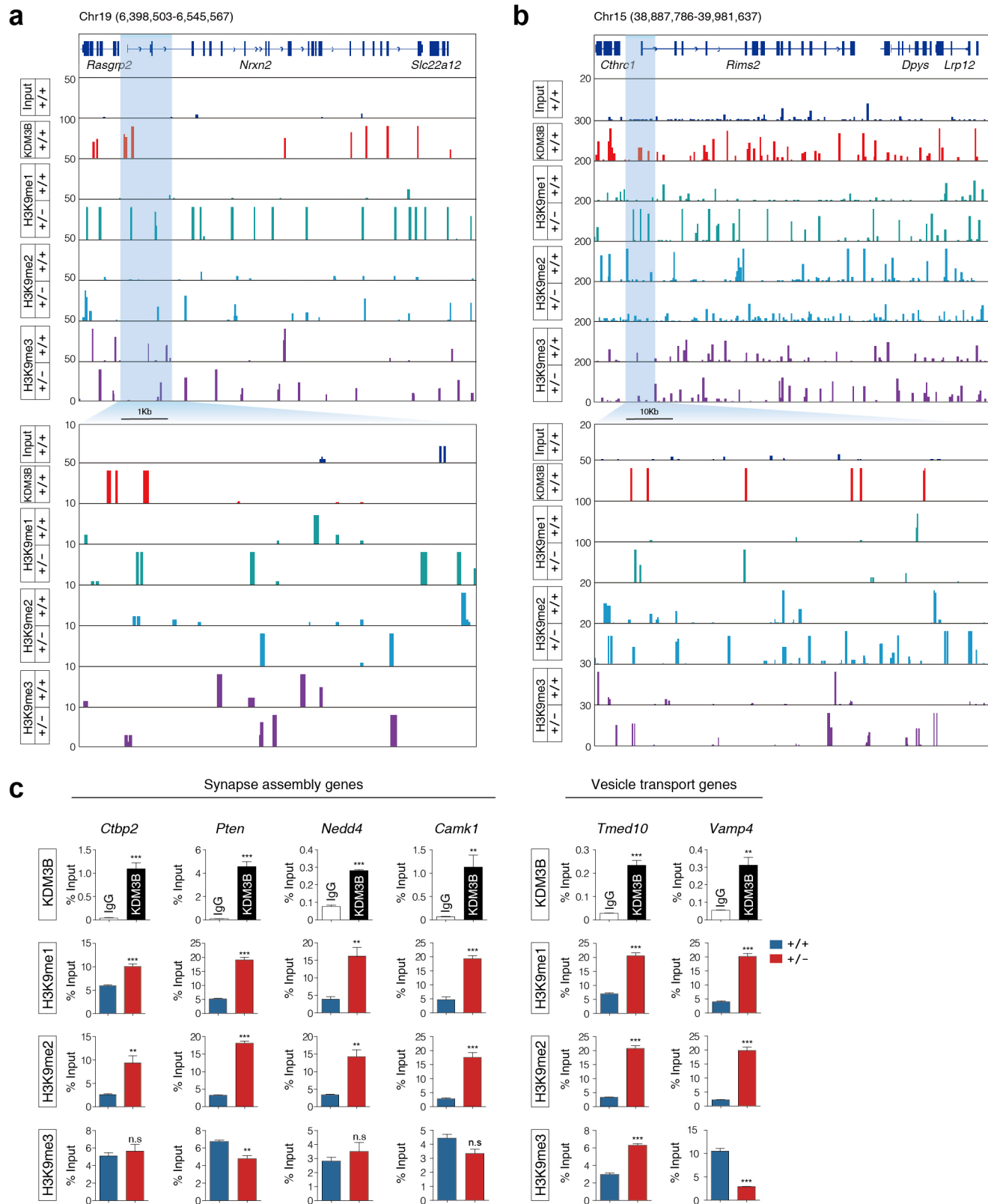
Extended Data Fig. 7 The alteration of synaptic morphology of cone photoreceptors in *Kdm3b*^{+/-} mice retina. **a**, TEM images of ribbon synapse in rod spherules and cone pedicles of 12-month-old *Kdm3b*^{+/+} and *Kdm3b*^{+/-} mice. Scale bar: 0.2 μm. **b**, Measurements of the length of ribbon synapses (μm) (left) and diameter of vesicles (μm) (right) by ImageJ software. Error bars show mean ± SEM. P values obtained by Student's t-test. ** P < 0.01, n.s., not significant. **c-e**, Representative scotopic ERGs elicited from 3- (**c**), 6- (**d**), and 12- (**e**) month-old *Kdm3b*^{+/+} and *Kdm3b*^{+/-} mice. **f-h**, Representative photopic ERGs elicited from 3- (**f**), 6- (**g**), and 12- (**h**) month-old *Kdm3b*^{+/+} and *Kdm3b*^{+/-} mice. **i**, Quantification of ERG responses at 1.2 log₁₀ cd.sec/m² light intensity from 3-, 6-, and 12-month-old *Kdm3b*^{+/+} and *Kdm3b*^{+/-} mice. Graphs show the mean ± SEM, and data are representative of n > 3 per each genotype. P values obtained by Student's t-test. ** P < 0.01, n.s., not significant.

Extended Data Fig. 8



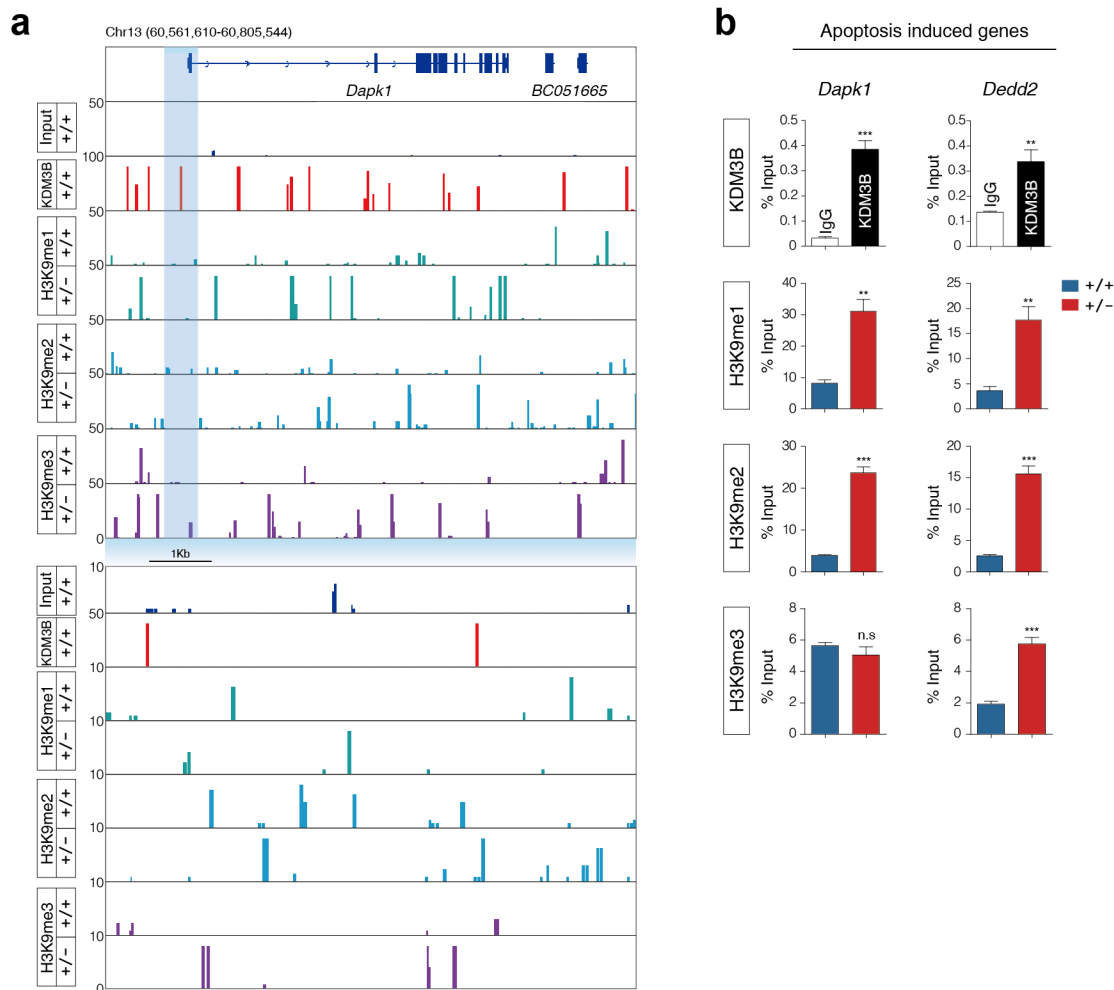
Extended Data Fig. 8 KDM3B is required for global H3K9 demethylation in mouse retinas. **a, b**, Bar graph shows the distribution of H3K9me1, H3K9me2, and H3K9me3 peaks around transcriptional start sites (left). Pie chart of H3K9me1, H3K9me2, and H3K9me3 enrichment distribution at genomic loci (right) in *Kdm3b*^{+/+} (**a**) and *Kdm3b*^{+/-} (**b**) mouse retinas.

Extended Data Fig. 9



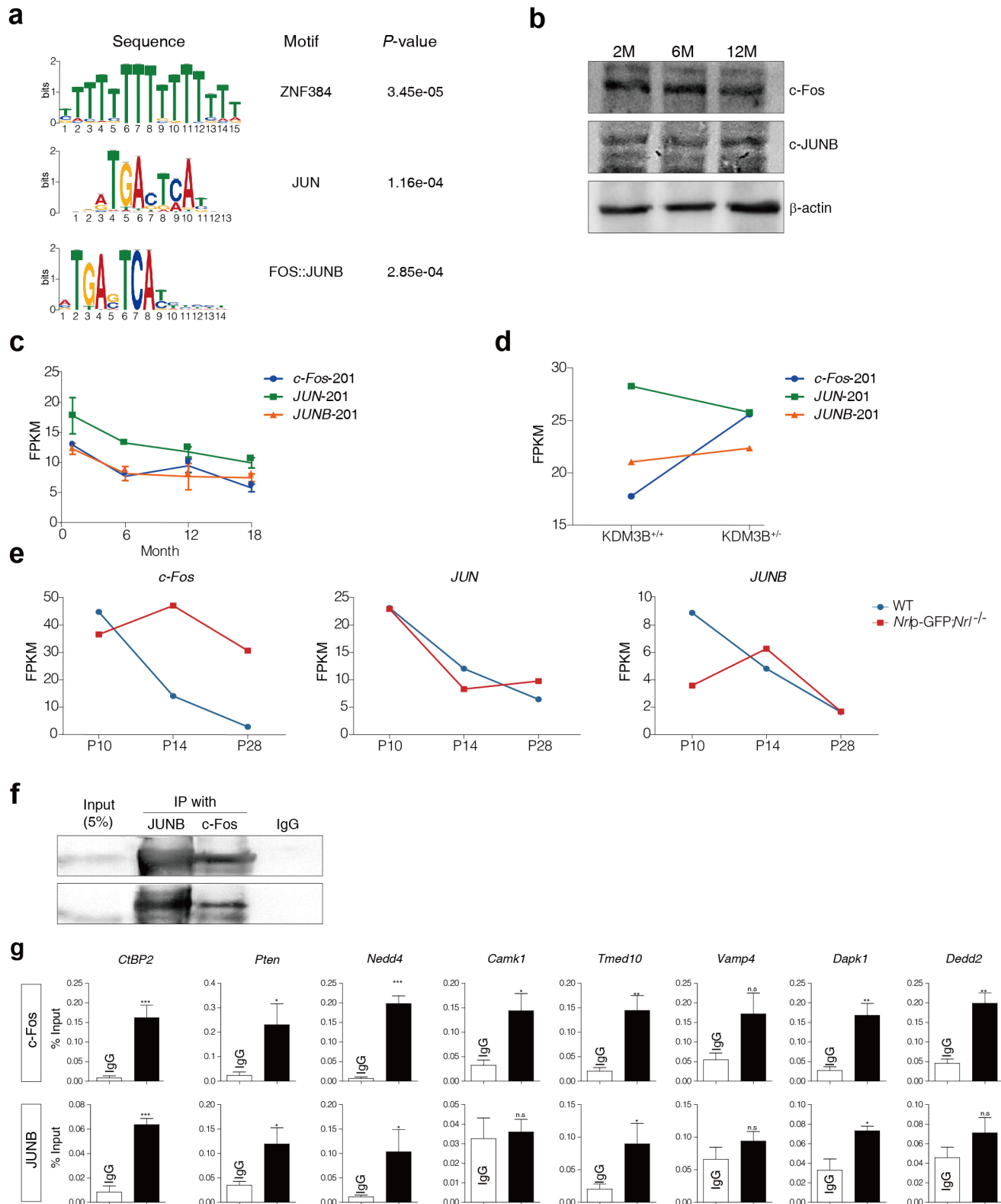
Extended Data Fig. 9 KDM3B regulates synapse assembly genes via erasing H3K9me1 and H3K9me2 marks. **a, b**, ChIP-seq tracks of KDM3B in *Kdm3b*^{+/+} and H3K9me1, H3K9me2, and H3K9me3 peaks in *Kdm3b*^{+/+} and *Kdm3b*^{+/-} mouse retinas along the *Nrxn2* (**a**) and *Rims2* (**b**) locus. Selected genomic elements (shaded with light cyan) indicate KDM3B ChIP-seq peaks at *Nrxn2* and *Rims2* promoter regions. **c**, Recruitment and presence of KDM3B, H3K9me1, H3K9me2, and H3K9me3 at indicated target gene promoters were validated by ChIP-qPCR. Error bars show mean \pm SEM. *P* values obtained by Student's t-test. *** *P* < 0.001, ** *P* < 0.01, n.s, not significant.

Extended Data Fig. 10



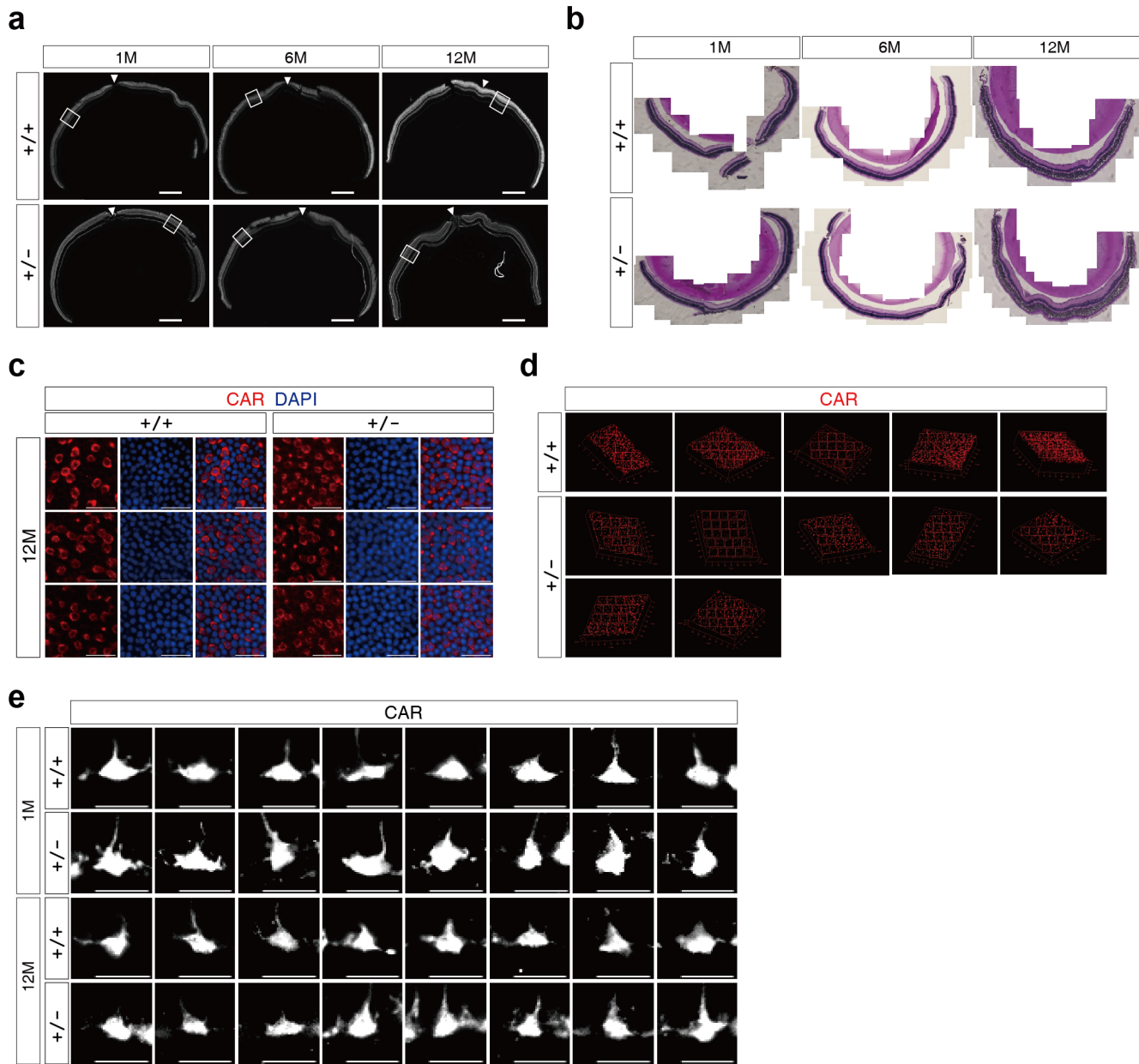
Extended Data Fig. 10 KDM3B regulates synapse assembly genes via erasing H3K9me1 and H3K9me2 marks. **a**, ChIP-seq tracks of KDM3B in *Kdm3b*^{+/+} and H3K9me1, H3K9me2, and H3K9me3 peaks in *Kdm3b*^{+/+} and *Kdm3b*^{+/-} mouse retinas along the *Dapk1* locus. Selected genomic element (shaded with light cyan) indicates KDM3B ChIP-seq peaks at *Dapk1* promoter region. **b**, Recruitment and presence of KDM3B, H3K9me1, H3K9me2, and H3K9me3 at apoptotic gene promoters were validated by ChIP-qPCR. Error bars show mean \pm SEM. *P* values obtained by Student's t-test. *** *P* < 0.001, ** *P* < 0.01, n.s., not significant.

Extended Data Fig. 11



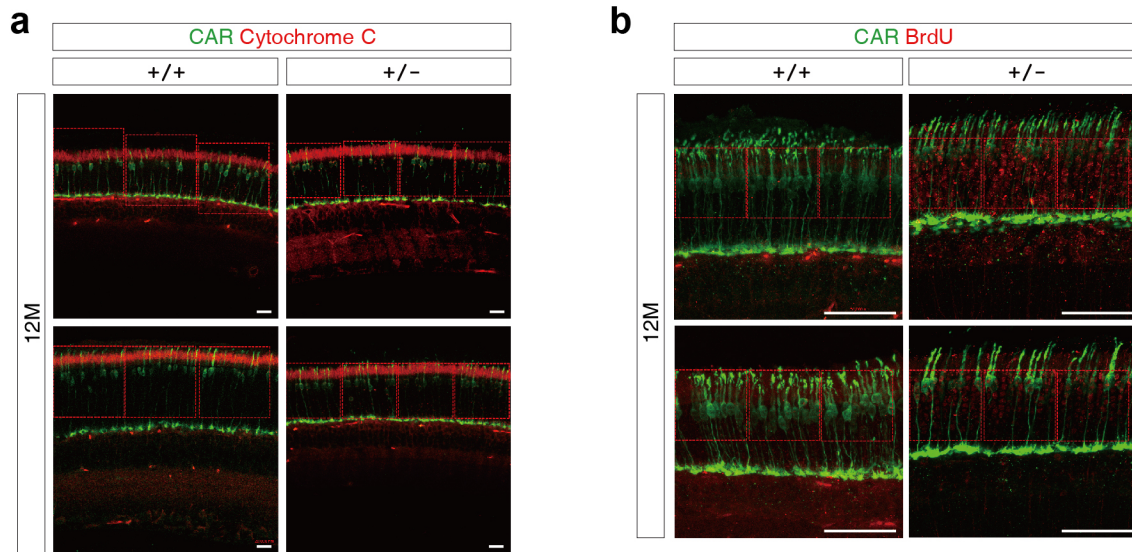
Extended Data Fig. 11 The AP-1 transcription factors are associated with KDM3B in mice retinas. **a**, The sequence logos representation of the 2 motifs identified using MEME-ChIP. De novo motif analysis was performed using sequences within a ± 150 bp window of KDM3B ChIP-Seq peaks. The sequence logo size indicates nucleotide frequency and the P-values represent the significance of motif enrichments compared to that of the genomic background. **b**, Whole retinal lysates of 2-, 6-, and 12-month-old mice were immunoblotted using anti-c-Fos and JUNB antibodies. β -actin was used for internal loading control. **c**, The expression level of *Kdm3b*, c-Fos, JUN, and JUNB transcripts in whole retina plotted for four developmental time points (1.5-, 3-, 6-, and 12-month-old). **d**, The expression level of *Kdm3b*, c-Fos, JUN, and JUNB transcripts in *Kdm3b*^{+/+} and *Kdm3b*^{+/-} mice retinas. **e**, The expression level of c-Fos, JUN, and JUNB transcripts in rod cell and s-cone-like cells (*Nrlp-GFP;Nrl*^{-/-}) plotted for three developmental time points (P10, P14, and P28) using public RNA-sequencing data (GSE 74660). **f**, Immunoblot showing co-immunoprecipitation of endogenous KDM3B with c-Fos and JUNB in human lung cancer cells. **g**, Recruitment and presence of c-Fos and JUNB at indicated gene promoters were validated by ChIP-qPCR. Error bars show mean \pm SEM. P values obtained by Student's t-test. *** $P < 0.001$, ** $P < 0.01$, n.s., not significant.

Supplementary Data Fig. 1



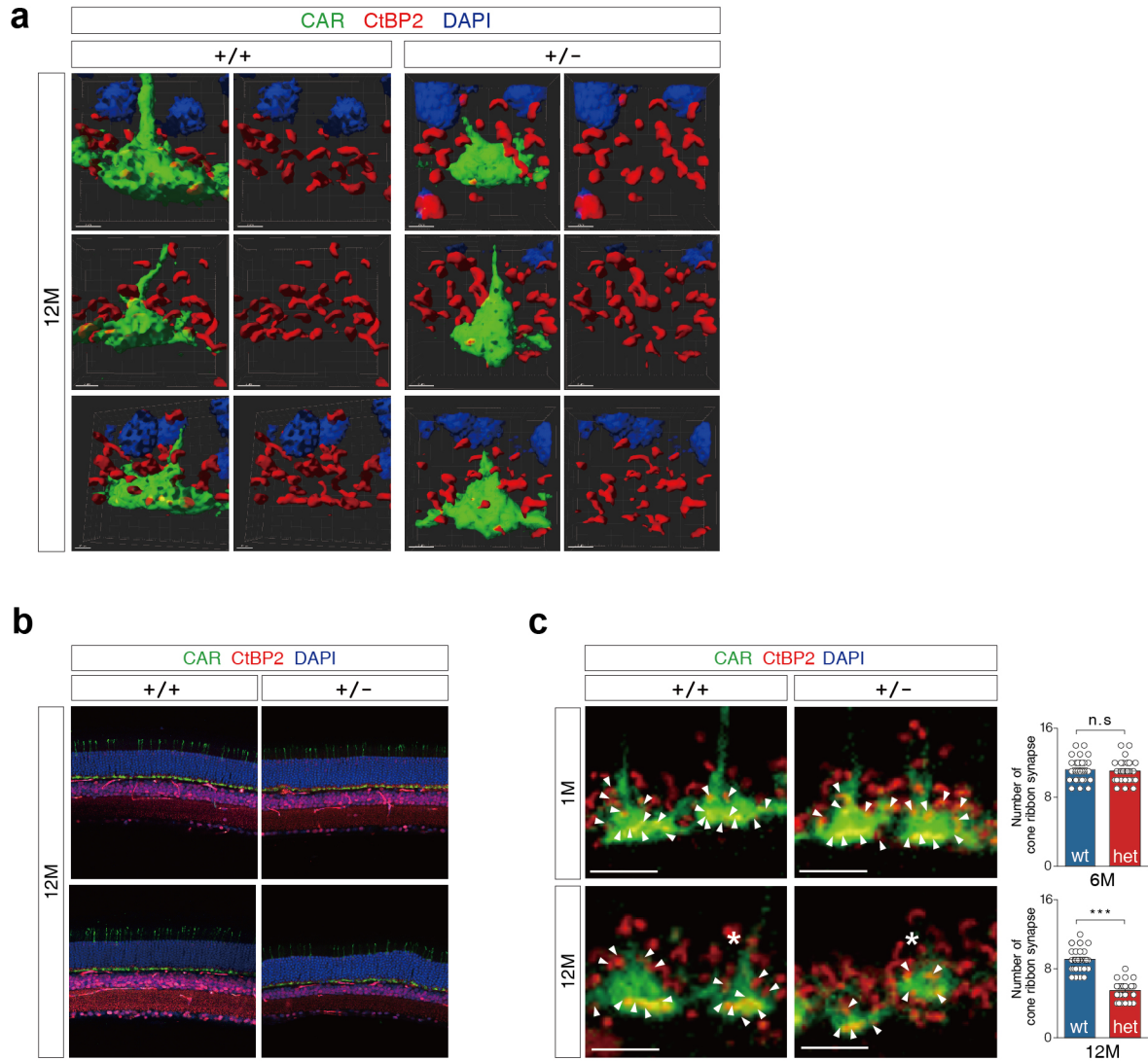
Supplementary Fig. 1 The morphological changes of rods and cones in *Kdm3b*^{+/+} and *Kdm3b*^{+/-} mouse retina. **a**, Cross-sectioned retinas were stained with DAPI from 1-, 6-, and 12-month-old *Kdm3b*^{+/+} and *Kdm3b*^{+/-} mice. Scale bar: 500 μ m. **b**, Representative images of hematoxylin and eosin (H&E) staining for retinal thickness and total number of nuclei in ONL, INL, and GCL in the retinas of 1-, 6-, and 12-month-old *Kdm3b*^{+/+} and *Kdm3b*^{+/-} mice. **c,d**, Immunostaining with CAR antibodies (red) of whole mount retina and DAPI (blue) in 12-month-old *Kdm3b*^{+/+} and *Kdm3b*^{+/-} mice. Scale bar: 20 μ m. **e**, The magnification of the cone pedicles in 1- and 12-months-old *Kdm3b*^{+/+} and *Kdm3b*^{+/-} mice. Scale bar: 10 μ m.

Supplementary Data Fig. 2



Supplementary Fig. 2 Induced apoptotic response of cone photoreceptors in $Kdm3b^{+/-}$ retinas. **a**, Immunostaining of cytochrome c (red) and CAR (green) in 12-month-old $Kdm3b^{+/+}$ and $Kdm3b^{+/-}$ retinas. Scale bar: 20 μm . Cytochrome c-intensity is measured in red dashed box. **b**, Apoptotic cells were detected by TUNEL assay (BrdU positive cells) in 12-month-old $Kdm3b^{+/+}$ and $Kdm3b^{+/-}$ mouse retinas. Scale bar: 50 μm . BrdU-positive cones in red dashed box are quantified.

Supplementary Data Fig. 3



Supplementary Fig. 3 The alteration of synaptic morphology of cone photoreceptors in *Kdm3b*^{+/-} mice retina. a, Immunostaining of Cone arrestin (CAR) and CtBP2 in 12-month-old *Kdm3b*^{+/+} and *Kdm3b*^{+/-} mouse retina sections. Scale bar: 2 μ m. **b**, The number of ribbon synapses in cone photoreceptor is quantified in 1- and 12-month-old *Kdm3b*^{+/+} and *Kdm3b*^{+/-} mouse retinas (n = 30) Scale bar: 20 μ m. **c**, 3D reconstruction images showing ribbon synapses in cone photoreceptors of 12-month-old *Kdm3b*^{+/+} and *Kdm3b*^{+/-} mouse retinas. Scale bar: 5 μ m

Supplementary Files

This is a list of supplementary files associated with this preprint. Click to download.

- [Supplementaryvideo1MP4.mp4](#)
- [Supplementaryinformation220103.docx](#)
- [SupplementaryTables.xlsx](#)
- [Supplementaryvideo2MP4.mp4](#)